EFFECTS OF ANISOTROPY UPON THE NORMAL MODES

by

K. J. Ellefsen, C. H. Cheng, and M. N. Toksöz

Earth Resources Laboratory
Department of Earth, Atmospheric, and Planetary Sciences
Massachusetts Institute of Technology
Cambridge, MA 02139

ABSTRACT

The effects of anisotropy upon elastic wave propagation along a fluid-filled cylindrical borehole are determined. The wave equation is solved in the frequency-wavenumber domain with a variational method, and the solution yields the phase velocities, group velocities, pressures, and displacements for the normal modes. These properties are studied for two cases: a transversely isotropic model for which the borehole has several different orientations with respect to the symmetry axis and an orthorhombic model for which the borehole is parallel to the intersection of two symmetry planes. The normal modes for these two cases show several significant effects which do not exist when the solid is isotropic or transversely isotropic with its symmetry axis parallel to the borehole:

1. The phase velocities for the quasi-pseudo-Rayleigh, both quasi-flexural, and both quasi-screw waves do not exceed the phase velocity of the slowest qS-wave. (The phase velocities of the leaky modes, which were not investigated, will exceed this threshold.)

2. The two quasi-flexural waves have different phase and group velocities; the differences are greatest at low frequencies and diminish as the frequency increases. The two quasi-screw waves behave similarly.

3. The greater the difference between the phase velocities of the qS-waves, the greater the difference between the phase velocities of the quasi-flexural waves at all frequencies. The two quasi-screw waves behave similarly.

4. Near the limiting qS-wave velocity, the difference between the phase velocities of the two quasi-flexural waves is greater than that for the two quasi-screw waves.

5. For the slow quasi-flexural wave, the particle displacements in the plane perpendicular to the borehole, when viewed together, are aligned with the polarization of the slow qS-wave.

6. For the fast quasi-flexural wave, the particle displacements in the plane perpendicular to the borehole, when viewed together, are aligned with the polarization of the fast qS-wave.

7. For the slow quasi-screw wave, the particle displacements in the plane perpendicular to the borehole, when viewed together, are aligned along two mutually perpendicular directions which are rotated 45° with respect to the polarizations of both qS-waves.

8. For the fast quasi-screw wave, the particle displacements in the plane perpendicular to the borehole, when viewed together, are aligned along two mutually perpendicular directions which are parallel with the polarizations of both qS-waves.

(In this list, the qS-waves are those plane waves whose wavenumber vectors are parallel to the borehole.) Despite these significant effects, the general characteristics of the phase and group velocities, pressures, and displacements are similar (but not identical) to those that would exist if the solid were isotropic or transversely isotropic with its symmetry axis parallel to the borehole. This result is expected because the models are only slightly anisotropic.

INTRODUCTION

Because many geophysicists believe that the crust of the Earth is slightly anisotropic, several research groups have studied how it affects the waves generated during acoustic logging. Tongtaow (1980), White and Tongtaow (1981), Tongtaow (1982), Chan and Tsang (1983), and Schmitt (1989) focused on the special case of transverse isotropy with the symmetry axis aligned with the borehole. White and Tongtaow studied the waves generated by monopole and dipole sources and determined what affects the velocities and amplitudes of the refracted and guided waves. Chan and Tsang examined the amplitudes and velocities of the refracted waves in concentrically-layered, transversely isotropic formations. Schmitt studied the velocity dispersion curves, the attenuation curves, and the frequency-dependent sensitivities for the normal modes when the formation is transversely isotropic and permeable. Recently, some researchers have focused on transverse isotropy when the symmetry axis is perpendicular to the borehole. Leveille and Seriff (1989) determined the particle motion of the tube wave at the zero frequency limit, and they studied the horizontal displacement on the inner wall of a finite length, cylindrical shell which has been excited by a horizontal point

force. Nicoletis et al. (1990) determined the phase velocity and particle displacements of a tube wave at the zero frequency limit.

No complete investigation has been performed for wave propagation in a borehole when the formation is transversely isotropic and the symmetry axis is not aligned with the borehole or when the formation has more general anisotropy. Consequently this paper is devoted to solving the wave equation and to studying the behavior of the normal modes for these complicated cases. The solution is derived in the frequency-wavenumber domain and is based upon a variational method which uses a combination of analytical expressions and finite elements. Although investigators in other disciplines have used a similar approach to solve the wave equation in anisotropic media (Nelson et al., 1971; Nelson, 1973; Huang and Dong, 1984; and Kausel, 1984), the solution for this problem is significantly more complicated for two reasons: (1) the wave equation must be solved for a cylindrical geometry when the anisotropy of the formation is defined in the Cartesian coordinate system, and (2) a fluid is present. With this solution, phase velocities, group velocities, and displacements are analyzed to determine how the anisotropy affects the normal modes.

Although only one problem is studied in this paper, the variational method developed here can be readily adapted to study many problems. The mesh can be altered to model a borehole with a highly irregular cross section which might be caused, for example, by a breakout (see e.g., Zoback et al., 1985). Additional fluid and solid layers can be added to model a cased borehole, a borehole with a tool in the center, and even a borehole with a tool which is not in the center. Wave propagation in an infinite rod which is heterogeneous and anisotropic and which has an irregular cross section (a topic which is important to the engineering community; Redwood, 1960; Miklowitz, 1978; Thurston, 1978) can be studied easily. Because these problems can be solved with minor modifications of the method developed here, this paper should be interesting to a wide audience.

METHOD

This section is devoted to developing a solution to the wave equation for the situation which exists during acoustic logging. First a mathematical model of the borehole environment is developed; then a variational equation which describes wave propagation in the borehole is formulated; and finally the variational equation is solved with the finite element method. Since many variables are needed in this section, they are listed in Tables 1 and 2 for easy reference. All tensors are expressed with abbreviated subscript notation.

Formulation

The model for the borehole environment consists of a perfectly elastic fluid in a cylindrical borehole through a perfectly elastic, homogeneous solid (Figure 1). The fluid and solid extend to infinity along the axis of the borehole, and the solid extends to infinity away from the borehole. The z axis of the coordinate system is in the center of the borehole, and the borehole radius is R.

The usual approach to solving related problems in wave propagation involves developing the solution to the wave equation in each layer and then matching the continuity conditions at the interfaces between the layers (see e.g., Kennett, 1983, Chapter 2). Using this approach for the borehole model would require solving the wave equation in cylindrical coordinates for the solid whose anisotropy is defined in Cartesian coordinates (e.g., transverse isotropy with any orientation of the symmetry axis and orthorhombic anisotropy). Using the separation of variables technique, the propagation in the z direction may be described by $\exp(ik_z z)$ where k_z is the wavenumber in the z direction. However, the anisotropy prevents the solution from being separable in r and θ. To overcome this problem of inseparability, a variational method can be used.

The variational method is based upon Hamilton's Principle. This principle is formulated with the Lagrangian energy which is defined as the kinetic energy of a system minus the potential energy of a system. In wave propagation problems, these energy terms are usually formulated with displacements (see e.g., Lysmer, 1970; Lysmer and Drake, 1972; Kausel and Roësset, 1981); however, when a fluid is present, the finite element solution to the variational equation works better when the energy terms for the fluid are formulated with a velocity potential, ϕ:

$$\nabla\phi = -\dot{\mathbf{u}} \tag{1}$$

where $\dot{\mathbf{u}}$ is the particle velocity (Everstine, 1981; Olsen and Bathe, 1985a). For this reason, the variational equation will be developed with three parts: one that pertains only to the fluid and is formulated with the velocity potential, another that pertains only to the solid and is formulated with displacements, and a third that involves the coupling at the fluid-solid interface.

For the fluid, the kinetic energy density is $\rho_1 \dot{\mathbf{u}}^T \dot{\mathbf{u}}/2$ where ρ_1 is the fluid density. Using Eq. (1), the kinetic energy is

$$\int_{V_1} dV \frac{1}{2}\rho_1 (\nabla\phi)^T \nabla\phi \tag{2}$$

where V_1 is the fluid volume. The potential energy density of the fluid is $\lambda_1 \Theta^2/2$ where λ_1 is the incompressibility and Θ is the dilatation (Bullen, 1963, p. 26). To expresses

this energy density in terms of ϕ, several algebraic substitutions must be made. The dilatation is defined as

$$\Theta = \nabla \cdot \mathbf{u} \tag{3}$$

(Bullen, 1963, p. 17) and using Eq. (1) its temporal derivative is

$$\dot{\Theta} = -\nabla^2 \phi \quad . \tag{4}$$

Using the wave equation for the fluid,

$$\nabla^2 \phi = \frac{\rho_1}{\lambda_1} \ddot{\phi} \tag{5}$$

where λ_1/ρ_1 is the square of the velocity (Lamb, 1879, section 287), the dilatation is expressed in terms of the potential:

$$\Theta = -\frac{\rho_1}{\lambda_1} \dot{\phi} \quad . \tag{6}$$

Therefore, the potential energy of the fluid is

$$\int_{V_1} dV \frac{1}{2} \frac{\rho_1^2}{\lambda_1} \dot{\phi}^2 \quad . \tag{7}$$

For the solid, the kinetic energy is derived by integrating the kinetic energy density over the volume of the solid:

$$\int_{V_2} dV \frac{1}{2} \rho_2 \dot{\mathbf{u}}^T \dot{\mathbf{u}} \tag{8}$$

where ρ_2 is the density of the solid and V_2 is the volume. The potential energy is derived similarly:

$$\int_{V_2} dV \frac{1}{2} \mathbf{E}^T \mathbf{C} \mathbf{E} \tag{9}$$

where $\mathbf{E}$ is the strain and $\mathbf{C}$ is the stiffness matrix.

The coupling at the fluid-solid interface is expressed in the variational equation in terms of work. The pressure at the interface,

$$p = -\lambda_1 \Theta \quad , \tag{10}$$

(Bullen, 1963, p. 23) is expressed in terms of the potential using Eq. (6):

$$p = \rho_1 \dot{\phi} \quad . \tag{11}$$

The traction exerted on the fluid by the solid equals the negative of the pressure times the normal, $\mathbf{n}$, which points into the solid: $-\rho_1 \dot{\phi} \mathbf{n}$. The force on the fluid with

an infinitesimal area, dS, equals the traction times dS. The work on the fluid is the surface integral of the inner product of the force and the displacement:

$$-\int_{\Sigma}^{\text{fluid}} dS\rho_1\dot{\phi}u_N \tag{12}$$

where Σ is the surface and u_N has replaced $\mathbf{n}\cdot\mathbf{u}$. The work on the solid at the interface is the negative of the work on the fluid:

$$\int_{\Sigma}^{\text{solid}} dSu_N\rho_1\dot{\phi} \quad . \tag{13}$$

The Lagrangian energy for the entire model is formed from the energy terms for the fluid, solid, and fluid-solid interface:

$$\begin{aligned} L \;=\; & \int_{V_1} dV\frac{1}{2}\rho_1(\nabla\phi)^T\nabla\phi - \int_{V_1} dV\frac{1}{2}\frac{\rho_1^2}{\lambda_1}\dot{\phi}^2 + \\ & \int_{V_2} dV\frac{1}{2}\rho_2\dot{\mathbf{u}}^T\dot{\mathbf{u}} - \int_{V_2} dV\frac{1}{2}\mathbf{E}^T\mathbf{C}\mathbf{E} - \\ & \int_{\Sigma}^{\text{fluid}} dS\rho_1\dot{\phi}u_N + \int_{\Sigma}^{\text{solid}} dSu_N\rho_1\dot{\phi} \quad . \end{aligned} \tag{14}$$

Notice that the net energy at the interface is zero. Hamilton's Principle states that the time integral of the Lagrangian energy is stationary for perturbations in the configuration of the system which satisfy the boundary conditions and which are specified at the initial and final times:

$$0 = \delta\int_{t_1}^{t_2} dtL \tag{15}$$

(see e.g., Lanczos, 1970, p. 111-114; Goldstein, 1980, p. 35-37). The initial and final times, t_1 and t_2, are arbitrary. To find the variational equation which describes wave propagation, substitute Eq. (14) into Eq. (15) and integrate by parts:

$$\begin{aligned} 0 \;=\; & \int_{t_1}^{t_2} dt\left(\int_{V_1} dV\rho_1(\nabla\delta\phi)^T\nabla\phi + \int_{V_1} dV\frac{\rho_1^2}{\lambda_1}\delta\phi\ddot{\phi} - \int_{V_2} dV\rho_2\delta\mathbf{u}^T\ddot{\mathbf{u}} - \right. \\ & \left. \int_{V_2} dV\delta\mathbf{E}^T\mathbf{C}\mathbf{E} + \int_{\Sigma}^{\text{fluid}} dS\rho_1\delta\phi\dot{u}_N + \int_{\Sigma}^{\text{solid}} dS\delta u_N\rho_1\dot{\phi}\right) - \\ & \int_{V_1} dV\frac{\rho_1^2}{\lambda_1}\phi\delta\phi\Big|_{t_1}^{t_2} + \int_{V_2} dV\rho_2\delta\dot{\mathbf{u}}^T\delta\mathbf{u}\Big|_{t_1}^{t_2} - \int_{\Sigma}^{\text{fluid}} dS\rho_1u_N\delta\phi\Big|_{t_1}^{t_2} \quad . \end{aligned} \tag{16}$$

Note that $\delta\mathbf{E}$ refers to perturbations in displacement. By convention, the perturbations in the configuration of the system (i.e., the potentials and the displacements) at t_1 and

t_2 are zero: $\delta\phi(t_1) = \delta\phi(t_2) = 0$ and $\delta\mathbf{u}(t_1) = \delta\mathbf{u}(t_2) = 0$. With these simplifications, the final equation, which is called the variational equation, is

$$\begin{aligned} 0 \;=\; \int_{t_1}^{t_2} dt \Bigg(& \int_{V_1} dV \rho_1 (\nabla\delta\phi)^T \nabla\phi + \int_{V_1} dV \frac{\rho_1^2}{\lambda_1} \delta\phi\ddot{\phi} - \\ & \int_{V_2} dV \rho_2 \delta\mathbf{u}^T \ddot{\mathbf{u}} - \int_{V_2} dV \delta\mathbf{E}^T \mathbf{C}\mathbf{E} + \\ & \int_{\Sigma} dS \rho_1 \delta\phi \dot{u}_N + \int_{\Sigma} dS \delta u_N \rho_1 \dot{\phi} \Bigg) \quad . \end{aligned} \tag{17}$$

The labels, "fluid" and "solid", have been dropped from the surface integrals because distinguishing between the work done on the fluid and the solid is not needed henceforth.

Solution

Discretization with Finite Elements

To solve the variational equation, expressions for the velocity potential, displacement, and strain must be developed. Because the wave equation is separable in z, propagation in this direction is described with $\exp(\imath k_z z)$. The wave equation is not separable in r and θ, and the finite element method is used to describe the velocity potentials and displacements in this plane. The horizontal plane is divided into small regions called elements, and the elements collectively form what is called the mesh (Figure 2). As a result of this discretization, the variational equation includes sums over the volumes of all elements and the surfaces between the elements at the fluid-solid interface:

$$\begin{aligned} 0 \;=\; \int_{t_1}^{t_2} dt \Bigg[& \sum_{m=1}^{M} \Bigg(\int_{V_1^{(m)}} dV^{(m)} \rho_1^{(m)} (\nabla\delta\phi^{(m)})^T \nabla\phi^{(m)} + \\ & \int_{V_1^{(m)}} dV^{(m)} \frac{\rho_1^{(m)2}}{\lambda_1^{(m)}} \delta\phi^{(m)} \ddot{\phi}^{(m)} \Bigg) - \\ & \sum_{n=1}^{N} \left(\int_{V_2^{(n)}} dV^{(n)} \rho_2^{(n)} \delta\mathbf{u}^{(n)T} \ddot{\mathbf{u}}^{(n)} + \int_{V_2^{(n)}} dV^{(n)} \delta\mathbf{E}^{(n)T} \mathbf{C}^{(n)} \mathbf{E}^{(n)} \right) + \\ & \sum_{q=1}^{Q} \left(\int_{\Sigma^{(q)}} dS^{(q)} \rho_1^{(q)} \delta\phi^{(q)} \dot{u}_N^{(q)} + \int_{\Sigma^{(q)}} dS^{(q)} \delta u_N^{(q)} \rho_1^{(q)} \dot{\phi}^{(q)} \right) \Bigg] \quad . \end{aligned} \tag{18}$$

where M, N, and Q are the numbers of fluid, solid, and interface elements, respectively, and m, n, and q are the associated indices. To solve this equation, expressions for the velocity potential, displacements, and strains must be developed for the finite elements.

Expressions for Velocity Potentioal, Displacement, and Strain

For a fluid element (Figure 3), the potentials are assigned at nine preselected points which are called nodes. (The potentials at these nodes are actually unknown at this stage and are calculated later.) The potential at a point within the element is calculated by interpolation. The interpolating functions for this wave propagation problem were chosen to be quadratic polynomials in x and y (Bathe, 1982, p. 200) because this order polynomial can approximate a reasonably complicated function without too much algebra. The potential at (x, y) within element m is a linear combination of the nine interpolating functions for the nine nodes:

$$\phi^{(m)}(x, y, z, t) = \frac{1}{2\pi} \int_{-\infty}^{\infty} dk_z \mathbf{h}^{(m)}(x, y) \mathbf{\Phi}^{(m)}(k_z, t) e^{\imath k_z z} \tag{19}$$

where $\mathbf{h}^{(m)}(x, y)$ is a row vector whose nine elements are the interpolation functions:

$$\mathbf{h}^{(m)}(x, y) = \begin{pmatrix} h_1^{(m)}(x, y) & h_2^{(m)}(x, y) & \cdots & h_9^{(m)}(x, y) \end{pmatrix} \quad ,$$

and $\mathbf{\Phi}^{(m)}(k_z, t)$ is a column vector with the nodal potentials:

$$\mathbf{\Phi}^{(m)}(k_z, t) = \begin{pmatrix} \Phi_1^{(m)}(k_z, t) \\ \Phi_2^{(m)}(k_z, t) \\ \vdots \\ \Phi_9^{(m)}(k_z, t) \end{pmatrix} \quad .$$

Note that Cartesian coordinates are used because the finite element method is actually easier to implement with them than with circular cylindrical coordinates. The fluid elements in the center of the mesh have six nodes (Figure 4), and the interpolating functions are also quadratic (Bathe, 1982, p. 230). The potential within this type of element is expressed with an equation like Eq. (19) except that $\mathbf{h}^{(m)}(x, y)$ and $\mathbf{\Phi}^{(m)}(k_z, t)$ only have six entries.

For a solid element, the three components of displacements are assigned at the nine nodes. The displacements at (x, y) within element n are

$$\mathbf{u}^{(n)}(x, y, z, t) = \frac{1}{2\pi} \int_{-\infty}^{\infty} dk_z \mathbf{H}^{(n)}(x, y) \mathbf{U}^{(n)}(k_z, t) e^{\imath k_z z} \tag{20}$$

where $\mathbf{H}^{(n)}(x,y)$ is 3×27 matrix:

$$\mathbf{H}^{(n)}(x,y) = \begin{pmatrix} h_1^{(n)}(x,y) & 0 & 0 \\ \vdots & \vdots & \vdots \\ h_9^{(n)}(x,y) & 0 & 0 \\ 0 & h_1^{(n)}(x,y) & 0 \\ \vdots & \vdots & \vdots \\ 0 & h_9^{(n)}(x,y) & 0 \\ 0 & 0 & h_1^{(n)}(x,y) \\ \vdots & \vdots & \vdots \\ 0 & 0 & h_9^{(n)}(x,y) \end{pmatrix}^T$$

and $\mathbf{U}^{(n)}(k_z,t)$ is a column vector with 27 elements:

$$\mathbf{U}^{(n)}(k_z,t) = \begin{pmatrix} U_{1x}^{(n)}(k_z,t) \\ \vdots \\ U_{9x}^{(n)}(k_z,t) \\ U_{1y}^{(n)}(k_z,t) \\ \vdots \\ U_{9y}^{(n)}(k_z,t) \\ U_{1z}^{(n)}(k_z,t) \\ \vdots \\ U_{9z}^{(n)}(k_z,t) \end{pmatrix} .$$

The expression for the displacements in the outermost elements is slightly different. Because their outer edges are located at infinite radius where the displacements are zero, nodes 1, 2, and 5 are not needed. Consequently $\mathbf{U}(k_z,t)$ has 18 elements, and $\mathbf{H}(x,y)$ is now a 3×18 matrix.

The strain at (x,y) within a solid element with nine nodes is

$$\mathbf{E}^{(n)}(x,y,z,t) = \frac{1}{2\pi} \int_{-\infty}^{\infty} dk_z \left(\mathbf{B}_0^{(n)}(x,y) + \imath k_z \mathbf{B}_1^{(n)}(x,y) \right) \mathbf{U}^{(n)}(k_z,t) e^{\imath k_z z} \quad . \qquad (21)$$

$\mathbf{B}_0^{(n)}(x,y)$ accounts for differentiation in the x and y directions, and its size is 6×27:

$$\mathbf{B}_0^{(n)}(x,y) = \begin{pmatrix} h_{1,x}^{(n)}(x,y) & 0 & 0 & 0 & 0 & h_{1,y}^{(n)}(x,y) \\ \vdots & \vdots & \vdots & \vdots & \vdots & \vdots \\ h_{9,x}^{(n)}(x,y) & 0 & 0 & 0 & 0 & h_{9,y}^{(n)}(x,y) \\ 0 & h_{1,y}^{(n)}(x,y) & 0 & 0 & 0 & h_{1,x}^{(n)}(x,y) \\ \vdots & \vdots & \vdots & \vdots & \vdots & \vdots \\ 0 & h_{9,y}^{(n)}(x,y) & 0 & 0 & 0 & h_{9,x}^{(n)}(x,y) \\ 0 & 0 & 0 & h_{1,y}^{(n)}(x,y) & h_{1,x}^{(n)}(x,y) & 0 \\ \vdots & \vdots & \vdots & \vdots & \vdots & \vdots \\ 0 & 0 & 0 & h_{9,y}^{(n)}(x,y) & h_{9,x}^{(n)}(x,y) & 0 \end{pmatrix}^T .$$

$\mathbf{B}_1^{(n)}(x,y)$ accounts for differentiation in the z direction, and its size is also 6×27:

$$\mathbf{B}_1^{(n)}(x,y) = \begin{pmatrix} 0 & 0 & 0 & 0 & h_1^{(n)}(x,y) & 0 \\ \vdots & \vdots & \vdots & \vdots & \vdots & \vdots \\ 0 & 0 & 0 & 0 & h_9^{(n)}(x,y) & 0 \\ 0 & 0 & 0 & h_1^{(n)}(x,y) & 0 & 0 \\ \vdots & \vdots & \vdots & \vdots & \vdots & \vdots \\ 0 & 0 & 0 & h_9^{(n)}(x,y) & 0 & 0 \\ 0 & 0 & h_1^{(n)}(x,y) & 0 & 0 & 0 \\ \vdots & \vdots & \vdots & \vdots & \vdots & \vdots \\ 0 & 0 & h_9^{(n)}(x,y) & 0 & 0 & 0 \end{pmatrix}^T .$$

For the outermost elements, $\mathbf{B}_0^{(n)}(x,y)$ and $\mathbf{B}_1^{(n)}(x,y)$ are both 6×18 because nodes 1, 2, and 5 are not included in the expression for the strain.

Along the fluid-solid interface, special elements are used (Figure 5). Locations within an element are specified by the distance along the interface, l. The potential at l in element q is

$$\phi^{(q)}(l,z,t) = \frac{1}{2\pi} \int_{-\infty}^{\infty} dk_z \mathbf{h}_I^{(q)}(l) \mathbf{\Phi}^{(q)}(k_z,t) e^{\imath k_z z} \quad . \tag{22}$$

$\mathbf{h}_I^{(q)}(l)$ is a row vector,

$$\mathbf{h}_I^{(q)}(l) = \begin{pmatrix} h_{I1}^{(q)}(l) & h_{I2}^{(q)}(l) & h_{I3}^{(q)}(l) \end{pmatrix} \quad ,$$

whose elements are interpolating functions developed from quadratic polynomials in l (Bathe, 1982, p. 199): $\mathbf{\Phi}^{(q)}(k_z,t)$ is a column vector whose elements are the potentials

at the three nodes:

$$\mathbf{\Phi}^{(q)}(k_z,t) = \begin{pmatrix} \Phi_1^{(q)}(k_z,t) \\ \Phi_2^{(q)}(k_z,t) \\ \Phi_3^{(q)}(k_z,t) \end{pmatrix} .$$

The normal displacement at l in element q is

$$u_N^{(q)}(l,z,t) = \frac{1}{2\pi}\int_{-\infty}^{\infty} dk_z \mathbf{H}_I^{(q)}(l)\mathbf{U}^{(q)}(k_z,t)e^{\imath k_z z} \tag{23}$$

where $\mathbf{U}^{(q)}(k_z,t)$ is a column vector whose elements are the components of the displacements at the three nodes:

$$\mathbf{U}^{(q)}(k_z,t) = \begin{pmatrix} U_{1x}^{(q)}(k_z,t) \\ U_{2x}^{(q)}(k_z,t) \\ U_{3x}^{(q)}(k_z,t) \\ U_{1y}^{(q)}(k_z,t) \\ U_{2y}^{(q)}(k_z,t) \\ U_{3y}^{(q)}(k_z,t) \end{pmatrix} .$$

The normal on the interface for node i is $(\cos\theta_i, \sin\theta_i)$ where θ_i is the angle that the normal makes with a line parallel to the x axis. $\mathbf{H}_I^{(q)}(l)$ is a row vector consisting of the interpolation functions and the appropriate components of the normal:

$$\mathbf{H}_I^{(q)}(l) = \begin{pmatrix} h_{I1}^{(q)}(l)\cos\theta_1 \\ h_{I2}^{(q)}(l)\cos\theta_2 \\ h_{I3}^{(q)}(l)\cos\theta_3 \\ h_{I1}^{(q)}(l)\sin\theta_1 \\ h_{I2}^{(q)}(l)\sin\theta_2 \\ h_{I3}^{(q)}(l)\sin\theta_3 \end{pmatrix}^T .$$

Note that $\mathbf{U}^{(q)}(k_z,t)$ does not contain any components of the displacements in the z direction because the normal to Σ is always perpendicular to the z direction.

Integrals in the Discretized Vairational Equation

To show how the integrals in the discretized variational equation are derived, the integral associated with the potential energy of the fluid will be derived in detail. Because the derivations for the other integrals are nearly identical, only the final results are presented.

The derivation of the integral associated with the potential energy of the entire fluid begins by computing the related integral for a fluid element. Eq. (19) is substituted into this integral:

$$\int_{V_1^{(m)}} dV^{(m)} \frac{\rho_1^{(m)2}}{\lambda_1^{(m)}} \delta\phi^{(m)} \ddot{\phi}^{(m)} = \tag{24}$$
$$\int dx \int dy \int_{-\infty}^{\infty} dz \frac{\rho_1^{(m)2}}{\lambda_1^{(m)}} \frac{1}{2\pi} \int_{-\infty}^{\infty} dk_z' \left[\mathbf{h}^{(m)}(x,y)\delta\Phi^{(m)}(k_z',t)\right]^T e^{\imath k_z' z}$$
$$\times \frac{1}{2\pi} \int_{-\infty}^{\infty} dk_z \mathbf{h}^{(m)}(x,y)\ddot{\Phi}^{(m)}(k_z,t) e^{\imath k_z z}$$

where the integrals over x and y only pertain to the domain of the element. The order in which the integrations are performed is changed:

$$\int_{V_1^{(m)}} dV^{(m)} \frac{\rho_1^{(m)2}}{\lambda_1^{(m)}} \delta\phi^{(m)} \ddot{\phi}^{(m)} = \frac{1}{(2\pi)^2} \int_{-\infty}^{\infty} dk_z \int_{-\infty}^{\infty} dk_z' \tag{25}$$
$$\times \delta\Phi^{(m)T}(k_z',t) \int dx \int dy \frac{\rho_1^{(m)2}}{\lambda_1^{(m)}} \mathbf{h}^{(m)T}(x,y)\mathbf{h}^{(m)}(x,y)\ddot{\Phi}^{(m)}(k_z,t) \int_{-\infty}^{\infty} dz e^{\imath(k_z+k_z')z} \quad .$$

To perform the integration over x and y, coordinates within the elements are calculated using the same interpolation functions which are used to calculate the potential. The result which is obtained with Gauss-Legendre quadrature (Bathe, 1982, p. 277-278) is a real, symmetric matrix:

$$\mathbf{M}_F^{(m)} = \int dx \int dy \frac{\rho_1^{(m)2}}{\lambda_1^{(m)}} \mathbf{h}^{(m)T}(x,y)\mathbf{h}^{(m)}(x,y) \quad . \tag{26}$$

The integral over z yields the Dirac delta function: $2\pi\delta(k_z + k_z')$ (Mathews and Walker, 1970, p. 102). The integral over k_z' is performed, and using the property that $\Phi^{(m)}(-k_z,t) = \Phi^{(m)*}(k_z,t)$ (Lathi, 1965, p. 111) the result is

$$\int_{V_1^{(m)}} dV^{(m)} \frac{\rho_1^{(m)2}}{\lambda_1^{(m)}} \delta\phi^{(m)} \ddot{\phi}^{(m)} = \frac{1}{2\pi} \int_{-\infty}^{\infty} dk_z \delta\Phi^{(m)H}(k_z,t)\mathbf{M}_F^{(m)}\ddot{\Phi}^{(m)}(k_z,t) \quad . \tag{27}$$

The vectors, $\Phi^{(m)}(k_z,t)$, and matrices, $\mathbf{M}_F^{(m)}$, for all elements are combined to form one vector, $\Phi(k_z,t)$ and one matrix, $\mathbf{M}_F$, for the entire model (Bathe, 1982, p. 124-125, 702-706). The final expression for the integral associated with the potential energy is

$$\sum_{m=1}^{M} \int_{V_1^{(m)}} dV^{(m)} \frac{\rho_1^{(m)2}}{\lambda_1^{(m)}} \delta\phi^{(m)} \ddot{\phi}^{(m)} = \frac{1}{2\pi} \int_{-\infty}^{\infty} dk_z \delta\Phi^H(k_z,t)\mathbf{M}_F\ddot{\Phi}(k_z,t) \quad . \tag{28}$$

The integral associated with the kinetic energy of the fluid is calculated in a similar manner using Eq. (19):

$$\sum_{m=1}^{M} \int_{V_1^{(m)}} dV^{(m)} \rho_1^{(m)} (\nabla \delta\phi^{(m)})^T \nabla \phi^{(m)} = \frac{1}{2\pi} \int_{-\infty}^{\infty} dk_z \delta\mathbf{\Phi}^H(k_z,t) \left(\mathbf{K}_{0F} + k_z^2 \mathbf{K}_{2F}\right) \mathbf{\Phi}(k_z,t) \quad . \tag{29}$$

where

$$\begin{aligned} \mathbf{K}_{0F}^{(m)} &= \int dx \int dy \rho_1 \left[\mathbf{h}_{,x}^{(m)T}(x,y)\mathbf{h}_{,x}^{(m)}(x,y) + \mathbf{h}_{,y}^{(m)T}(x,y)\mathbf{h}_{,y}^{(m)}(x,y)\right] \\ \mathbf{K}_{2F}^{(m)} &= \int dx \int dy \rho_1 \mathbf{h}^{(m)T}(x,y)\mathbf{h}^{(m)}(x,y) \quad . \end{aligned} \tag{30}$$

Matrices $\mathbf{K}_{0F}$ and $\mathbf{K}_{2F}$ are real and symmetric.

The integral associated with the potential energy of the solid is calculated with Eq. (21):

$$\sum_{n=1}^{N} \int_{V_2^{(n)}} dV^{(n)} \delta\mathbf{E}^{(n)T} \mathbf{C}^{(n)} \mathbf{E}^{(n)} = \frac{1}{2\pi} \int_{-\infty}^{\infty} dk_z \delta\mathbf{U}^H(k_z,t) \left(\mathbf{K}_{0S} + \imath k_z \mathbf{K}_{1S} + k_z^2 \mathbf{K}_{2S}\right) \mathbf{U}(k_z,t) \tag{31}$$

where

$$\begin{aligned} \mathbf{K}_{0S}^{(n)} &= \int dx \int dy\, \mathbf{B}_0^{(n)T}(x,y)\mathbf{C}^{(n)}\mathbf{B}_0^{(n)}(x,y) \\ \mathbf{K}_{1S}^{(n)} &= \int dx \int dy\, [\, \mathbf{B}_0^{(n)T}(x,y)\mathbf{C}^{(n)}\mathbf{B}_1^{(n)}(x,y) - \\ &\qquad \mathbf{B}_1^{(n)T}(x,y)\mathbf{C}^{(n)}\mathbf{B}_0^{(n)}(x,y)\,] \\ \mathbf{K}_{2S}^{(n)} &= \int dx \int dy\, \mathbf{B}_1^{(n)T}(x,y)\mathbf{C}^{(n)}\mathbf{B}_1^{(n)}(x,y) \quad . \end{aligned} \tag{32}$$

Matrices $\mathbf{K}_{0S}$ and $\mathbf{K}_{2S}$ are real and symmetric; Matrix $\mathbf{K}_{1S}$ is real and antisymmetric. For the outermost elements which extend to infinity in the radial direction, the integration over x and y is performed using the coordinate interpolation scheme given by Olsen and Bathe (1985b).

The integral associated with the kinetic energy of a solid element is calculated with Eq. (20):

$$\sum_{n=1}^{N} \int_{V_2^{(n)}} dV^{(n)} \rho_2^{(n)} \delta\mathbf{u}^{(n)T} \ddot{\mathbf{u}}^{(n)} = \frac{1}{2\pi} \int_{-\infty}^{\infty} dk_z \delta\mathbf{U}^H(k_z,t) \mathbf{M}_S \ddot{\mathbf{U}}(k_z,t) \tag{33}$$

where

$$\mathbf{M}_S^{(n)} = \int dx \int dy \rho_2 \mathbf{H}^{(n)T}(x,y)\mathbf{H}^{(n)}(x,y) \quad . \tag{34}$$

Matrix $\mathbf{M}_S$ is real and symmetric. Again, the coordinate interpolation scheme by Olsen and Bathe (Olsen, 1985b) is used for the integration over x and y for the outermost elements.

The integral associated with the work done on the fluid at the fluid-solid interface is computed with Eqs. (22) and (23):

$$\sum_{q=1}^{Q} \int_{\Sigma^{(q)}} dS^{(q)} \rho_1^{(q)} \delta\phi^{(q)} \dot{u}_N^{(q)} = \frac{1}{2\pi} \int_{-\infty}^{\infty} dk_z \delta\mathbf{\Phi}^H(k_z,t)\mathbf{F}\dot{\mathbf{U}}(k_z,t) \tag{35}$$

where

$$\mathbf{F}^{(q)} = \int dl \rho_1 \mathbf{h}_I^{(q)T}(l)\mathbf{H}_I^{(q)}(l) \quad . \tag{36}$$

Matrix $\mathbf{F}$ is real.

The integral associated with the work done on the solid at the fluid-solid interface is computed also with Eqs. (22) and (23):

$$\sum_{q=1}^{Q} \int_{\Sigma^{(q)}} dS^{(q)} \delta u_N^{(q)} \rho_1^{(q)} \dot{\phi}^{(q)} = \frac{1}{2\pi} \int_{-\infty}^{\infty} dk_z \delta\mathbf{U}^H(k_z,t)\mathbf{F}^T\dot{\mathbf{\Phi}}(k_z,t) \quad . \tag{37}$$

Wave Equation

The solution to the variational equation is obtained by substituting Eqs. (28), (29), (31), (33), (35), and (37) into Eq. (18), and the resulting equation is

$$0 = \int_{t_1}^{t_2} \frac{1}{2\pi} \int_{-\infty}^{\infty} dk_z \delta\mathbf{Y}^H \left[\left(\mathbf{A}_0 + k_z\mathbf{A}_1 + k_z^2\mathbf{A}_2 \right) \mathbf{V} + \mathbf{D}_1\dot{\mathbf{V}} + \mathbf{D}_2\ddot{\mathbf{V}} \right] \tag{38}$$

where

$$\begin{aligned}
\mathbf{Y} &= \begin{pmatrix} \mathbf{\Phi}(k_z,t) \\ \mathbf{U}(k_z,t) \end{pmatrix} \\
\mathbf{V} &= \begin{pmatrix} \mathbf{\Phi}(k_z,t) \\ -\mathbf{U}(k_z,t) \end{pmatrix} \\
\mathbf{A}_0 &= \begin{pmatrix} \mathbf{K}_{0F} & \mathbf{0} \\ \mathbf{0} & \mathbf{K}_{0S} \end{pmatrix} \\
\mathbf{A}_1 &= \begin{pmatrix} \mathbf{0} & \mathbf{0} \\ \mathbf{0} & \imath\mathbf{K}_{1S} \end{pmatrix}
\end{aligned} \tag{39}$$

$$\begin{aligned}
\mathbf{A}_2 &= \begin{pmatrix} \mathbf{K}_{2F} & \mathbf{0} \\ \mathbf{0} & \mathbf{K}_{2S} \end{pmatrix} \\
\mathbf{D}_1 &= \begin{pmatrix} \mathbf{0} & -\mathbf{F} \\ \mathbf{F}^T & \mathbf{0} \end{pmatrix} \\
\mathbf{D}_2 &= \begin{pmatrix} \mathbf{M}_F & \mathbf{0} \\ \mathbf{0} & \mathbf{M}_S \end{pmatrix} \quad .
\end{aligned}$$

For arbitrary perturbations, $\delta\mathbf{Y}$, the integral will be zero when

$$\left(\mathbf{A}_0 + k_z\mathbf{A}_1 + k_z^2\mathbf{A}_2\right)\mathbf{V} + \mathbf{D}_1\dot{\mathbf{V}} + \mathbf{D}_2\ddot{\mathbf{V}} = \mathbf{0} \quad , \tag{40}$$

and this equation is called the wave equation. In the frequency-wavenumber domain the wave equation is

$$\left(\mathbf{A}_0' + k_z\mathbf{A}_1 + k_z^2\mathbf{A}_2\right)\tilde{\mathbf{V}} = \mathbf{0} \tag{41}$$

where

$$\begin{aligned}
\tilde{\mathbf{V}} &= \begin{pmatrix} \Phi(k_z,\omega) \\ -\mathbf{U}(k_z, omega) \end{pmatrix} \\
\mathbf{A}_0' &= \begin{pmatrix} \mathbf{K}_{0F} - \omega^2\mathbf{M}_F & \imath\omega\mathbf{F} \\ -\imath\omega\mathbf{F}^T & \mathbf{K}_{0S} - \omega^2\mathbf{M}_S \end{pmatrix} \quad .
\end{aligned} \tag{42}$$

Matrices $\mathbf{A}_0'$ and $\mathbf{A}_1$ are Hermitian, and $\mathbf{A}_2$ is real and symmetric.

Eq. (41) is a quadratic eigenvalue problem — the eigenvalue is k_z, and the eigenvector is $\mathbf{V}$. The eigenvalues and eigenvectors are calculated using an algorithm developed by Chen and Taylor (1988), which has been modified for complex, Hermitian matrices. Each eigenvalue-eigenvector pair applies to one normal mode. The phase velocity, v, of the mode is calculated with $v = \omega/k_z$. The pressures in the fluid elements are calculated with Eqs. (11) and (19). The displacements in the solid elements are calculated with Eq. (20).

After the wave equation is solved, the group velocity can be readily calculated using only matrix multiplication. To derive the formula, Eq. (41) is differentiated with respect to k_z and multiplied on the left by $\mathbf{V}^H$. The equation is then solved for $\partial\omega/\partial k_z$, the group velocity:

$$U_G(k_z,\omega) = \frac{\partial\omega}{\partial k_z} = \frac{\mathbf{V}^H\left[\mathbf{A}_1 + 2k_z\mathbf{A}_2\right]\mathbf{V}}{\mathbf{V}^H\begin{pmatrix} 2\omega\mathbf{M}_F & -\imath\mathbf{F} \\ \imath\mathbf{F}^T & 2\omega\mathbf{M}_S \end{pmatrix}\mathbf{V}} \quad . \tag{43}$$

Discussion of the Method

The eigenvalue problem actually has four related solutions. The obvious solution for a normal mode may be represented by the combination: ω, k_z, $\tilde{\mathbf{V}}$. The solution for another mode propagating in the same direction is the combination: $-\omega$, $-k_z$, $\tilde{\mathbf{V}}^*$, and this result may be verified by manipulating Eq. (41). The solutions for the modes propagating in the opposite direction are ω, $-k_z$, $\tilde{\mathbf{Y}}$ and $-\omega$, k_z, $\tilde{\mathbf{Y}}^*$ where

$$\tilde{\mathbf{Y}} = \begin{pmatrix} \Phi(k_z,\omega) \\ \mathbf{U}(k_z,omega) \end{pmatrix} \quad . \tag{44}$$

These multiple solutions indicate that the phase velocities of the modes propagating in opposite directions along the borehole are equal, even if the solid has completely general anisotropy. Although this fact is surprising, plane waves demonstrate similar behavior: the phase velocities of two plane waves propagating in opposite directions in an anisotropic medium are always equal. (This property can be readily proven using the Christoffel equation (see e.g., Auld, 1973, p. 210-211).)

Two features of the variation equation make it amenable to a finite element solution. First, because the motion in the fluid is described in terms of a velocity potential instead of displacements, spurious modes do not develop (Wiggins, 1976; Hamdi and Ousset, 1978; Everstine, 1981; Buland and Gilbert, 1984; Olsen and Bathe, 1985a). This potential-based method has the added advantage that it needs far fewer equations than the displacement-based method. Second, the variational equation is formulated in terms of first spatial derivatives and not the second spatial derivatives which are in the wave equation (see e.g., Aki and Richards, 1980, p. 19). Consequently the potential and displacements calculated with this variational method approximate well the exact values of these quantities, a point which will be demonstrated later. For the strains and stresses, which involve first derivatives, the match between values obtained with the variational method and the exact values is not as good (see Carrier and Pearson, 1976, p. 175).

The combined use of analytical and numerical expressions for the velocity potential and displacement has two very important advantages. First, because the pressures and displacements for the modes are expressed in the frequency-wavenumber domain using $\exp[\imath(k_z z - \omega t)]$, some properties of their behavior such as velocity dispersion can be easily studied. Second, using $\exp(\imath k_z z)$ to simulate wave propagation in the z direction greatly reduces the size of the problem. If this analytical expression were not used, then a three-dimensional mesh would have to be established. Since the memory requirements for the two-dimensional mesh are quite large, the memory requirements for the three-dimensional mesh would be enormous. Concomitantly the number of computations would increase greatly. These two factors suggest that trying to solve the variational equation using a three-dimensional mesh might exceed the capabilities of current computers.

An important issue in the finite element method is designing the mesh. The mesh must have enough elements in the right locations to allow reasonably accurate wavenumbers, pressures, and displacements to be calculated. At the same time, the mesh must have as few elements as possible to minimize the amount of computation and memory needed to solve the wave equation. The selected mesh (Figure 2) satisfied these two criteria for the tube, pseudo-Rayleigh, flexural, and screw waves, which are the normal modes commonly encountered in acoustic logging. The mesh is very dense in the radial direction near the borehole wall because the pressures and displacements for the modes change rapidly here. The density is only high enough for the lower order radial modes; the higher order radial modes have even more rapid changes and would require more elements. Because the pressures and displacements change slowly away from the borehole wall, the mesh density is lower there. As the radial distance increases (beyond the borehole wall) the displacements for normal modes diminish and eventually go to zero at infinity. The outermost elements (Figure 2) model this behavior well; however, these elements cannot model the leaky modes which have oscillatory displacements. The mesh density in the azimuthal direction is just high enough to obtain accurate results for the tube and pseudo-Rayleigh waves which do not change with azimuth, for the flexural wave which changes according to $\cos\theta$, and for the screw wave which changes according to $\cos 2\theta$. Obtaining good results for a mode with a higher azimuthal order number would require more elements.

This variational method has been extensively tested, and the results are very accurate. Consider a model with an isotropic, fast formation (Table 3) and another with an isotropic, slow formation (Table 4) because exact solutions for the phase and group velocities, pressures, and displacements exist. The phase and group velocities calculated with the variational method are almost always within 0.1% of their exact values (Figures 6, 7, 8, and 9). Similarly the pressures and displacements calculated with the variational method match the exact solutions (Figures 10, 11, 12, and 13).

RESULTS

Although the behavior of the modes could be studied for many types of anisotropy, only those types which are prevalent in the Earth should be considered. Field data, laboratory data, and mathematical modeling indicate that two types are important. Transverse isotropy is a good model for (1) sedimentary rocks like shales which contain aligned clay minerals (Thomsen, 1986; Winterstein, 1986), (2) formations which consist of many beds that are thin relative to the wavelength of an elastic wave (Backus, 1962; White, 1955), and (3) rocks with aligned microfractures (Crampin, 1984). Orthorhombic anisotropy is a good model for some igneous and metamorphic rocks whose microcracks and minerals are aligned (Thill et al., 1973).

Different orientations of the borehole with respect to the anisotropy can model

different situations. For example, when the symmetry axis of a transversely isotropic medium is parallel to the borehole, acoustic logging in many sedimentary rocks is adequately modeled. When the symmetry axis is slightly tilted, a vertical borehole through a tilted, transversely isotropic formation or a deviated borehole through a horizontal, transversely isotropic formation is modeled. And when the symmetry axis is perpendicular to the borehole, a formation with aligned microcracks is modeled.

In this section, normal mode propagations in transversely isotropic and orthorhombic models are studied with the variational method. The accuracy of the phase velocities is checked using a perturbation method. Using the formula, $U_G = v\left[1 - \frac{\omega}{v}\frac{dv}{d\omega}\right]^{-1}$, (where v is the phase velocity computed with the perturbation method) the accuracy of the group velocities is checked.

Transversely Isotropic Models

Because the behavior of the normal modes in the transversely isotropic models is closely related to planar qS-wave propagation, these waves will be discussed first. The properties of the solid are listed in Table 5. The waves propagating parallel to the symmetry axis have the same phase velocity, 2.97 km/s (Figure 14a). Although the polarizations for this particular propagation direction are often decomposed into the orientations shown in Figure 14b, the orientations are actually arbitrary. The waves propagating at an angle with respect to the symmetry axis have different phase velocities and different polarizations with unique orientations. For example, when the propagation direction is 20° with respect to the symmetry axis, the phase velocities are 2.99 km/s and 3.03 km/s. The polarization of the slower wave is perpendicular to the a-b plane, and that for the faster wave is in this plane. When the propagation direction is 90° with respect to the symmetry axis, the phase velocities are 2.97 km/s and 3.17 km/s. The polarization of the faster wave is perpendicular to the a-b plane, and that for the slower wave is in this plane.

First, normal modes were computed when the symmetry axis was parallel to the borehole. The properties of the borehole model are listed in Table 5. The shapes of the phase and group velocity curves (Figures 15 and 16) are like those for an isotropic model. The phase velocities do not exceed 2.97 km/s which equals the phase velocities of the two S waves propagating parallel to the symmetry axis (Figure 14). The characteristics of the displacements and pressures are identical to those for an isotropic model and consequently are not plotted. The orientations of the two flexural waves and two screw waves are arbitrary just as the polarizations of the two S waves propagating parallel to the symmetry axis are arbitrary.

When the symmetry axis is tilted 20° and 90° with respect to the borehole, small

but significant changes occur in the phase and group velocities. (The modes are labeled with the same name used for isotropic models except that the prefix, quasi or q, is attached.) The general shapes of the dispersion curves are the same as those when the symmetry axis is aligned with the borehole (Figures 17, 18, 19, 20, 21, 22, 23, and 24). When the symmetry axis is tilted 20°, the phase velocities of the normal modes never exceed 2.99 km/s, the phase velocity of the slowest qS-wave whose wavenumber vector is parallel to the borehole. An analogous result applies when the symmetry axis is tilted 90°. In both cases, the quasi-flexural and quasi-screw waves have different phase and group velocities (Figures 25, 26, 27, 28); the differences are large at low frequencies but small at high frequencies. Near the limiting qS-wave velocity, the difference between the phase velocities for the quasi-flexural waves is greater than the difference between the phase velocities for the quasi-screw waves.

The most obvious effect of the anisotropy is the alignment of the quasi-flexural and quasi-screw waves. (Because the general characteristics of the displacements for the 20° and 90° models are similar, only the displacements for the 20° model are plotted.) For the slow quasi-flexural wave, the particle displacements in the plane perpendicular to the borehole, when viewed together, are aligned with the polarization of the slow qS-wave whose wavenumber vector is parallel to the borehole (Figure 29). For the fast quasi-flexural wave, the particle displacements in the plane perpendicular to the borehole, when viewed together, are aligned with the polarization of the fast qS-wave (Figure 30). For the slow quasi-screw wave, the particle displacements in the plane perpendicular to the borehole, when viewed together, are aligned along two mutually perpendicular directions which are rotated 45° with respect to the polarizations of the slow and fast qS-waves (Figure 31). For the fast quasi-screw wave, the particle displacements in the plane perpendicular to the borehole, when viewed together, are aligned along two mutually perpendicular directions which are parallel to the polarizations of the qS-waves (Figure 32). The quasi-tube and quasi-pseudo-Rayleigh waves show no obvious alignment with respect to the qS-waves (Figures 33 and 34). The anisotropy makes the displacements for each wave truly different from those that would exist if the solid were isotropic or transversely isotropic with its symmetry axis parallel to the borehole. However, these changes are so small that they are not discernible in Figures 29, 30, 31, 32, 33, and 34, and consequently a valid generalization is that the displacements are very similar to those which exist when the medium is isotropic or transversely isotropic with its symmetry axis parallel to the borehole.

Orthorhombic Model

For the orthorhombic model (Table 6) only one orientation of the borehole was studied: the borehole is parallel to the intersection of two symmetry planes. The phase velocities of the two qS-waves which propagate parallel to the borehole are 2.67 km/s and 2.95 km/s (Figure 35a), and their polarizations are mutually perpendicular (Figure 35b).

The phase and group velocities of the normal modes (Figures 36, 37, 38, and 37) are like those in the transversely isotropic models when the symmetry axis is tilted with respect to the borehole. The phase and group velocities do not exceed 2.67 km/s, the phase velocity of the slow qS-wave whose wavenumber vector is parallel to the borehole. The two quasi-flexural waves have different phase and group velocities, and the differences are large at low frequencies but small at high frequencies (Figures 40 and 42). The two quasi-screw waves behave similarly (Figures 41 and 42). Near the limiting qS-wave velocity, the difference between the phase velocities of the quasi-flexural waves is greater than that for the quasi-screw waves.

The displacements are also like those in the transversely isotropic models when the symmetry axis is tilted with respect to the borehole. (For this reason, they are not plotted.) For the slow quasi-flexural wave, the particle displacements in the plane perpendicular to the borehole, when viewed together, are aligned with the polarizations of the slow qS-wave whose wavenumber vector is parallel to the borehole. For the fast quasi-flexural wave, the particle displacements in the plane perpendicular to the borehole, when viewed together, are aligned with the polarization of the fast qS-wave. For the slow quasi-screw wave, the particle displacements in the plane perpendicular to the borehole, when viewed together, are aligned along two mutually perpendicular directions which are rotated 45° with respect to the polarizations of the slow and fast qS-waves. For the fast quasi-screw wave, the particle displacements in the plane perpendicular to the borehole, when viewed together, are aligned along two mutually perpendicular directions which are parallel with the polarizations of the two qS-waves. Due to the anisotropy the displacements are different from those that would exist if the solid were isotropic or transversely isotropic with its symmetry axis parallel to the borehole, but the differences are small.

Discussion of the Results

The differences in the phase and group velocities of the quasi-flexural and quasi-screw waves are correlated with the differences between the phase velocities of the qS-waves whose wavenumber vectors are parallel to the axis of the borehole. This result suggests that phase velocity surface can be used to predict the relative differences in the velocities of these two modes. For example, when the velocity surface shows that the differences between the two qS-waves are zero, the quasi-flexural waves will have the same phase and group velocities. When the surface shows a large difference, the two quasi-flexural waves will have a correspondingly large difference in their phase and group velocities. Using this property, the general behavior of the normal modes for virtually any model can be readily predicted.

SUMMARY AND CONCLUSIONS

A variational method was developed to calculate wavenumbers, pressures, and displacements for normal modes propagating along a fluid-filled borehole in an anisotropic medium. The implementation uses an analytical expression, $\exp(\imath k_z z)$, to describe wave propagation along the borehole and finite element expressions to describe propagation in the plane perpendicular to the borehole. This approach has two advantages: it reduces the size of the problem to the extent that current computers can perform the calculations, and it allows the modes to be expressed in the frequency-wavenumber domain where their modal behavior can be studied. For isotropic models, the phase and group velocities, pressures, and displacements calculated with this variational method matched exact solutions.

The investigation of the behavior of the normal modes in anisotropic models was limited to two cases: a transversely isotropic model for which the borehole had several different orientations with respect to the symmetry axis and an orthorhombic model for which the borehole was parallel to the intersection of two symmetry planes. These two cases were chosen because they adequately represent many logging situations. For these anisotropic models the phase and group velocities calculated with the variational method match those calculated with a completely independent method based upon perturbation theory.

The normal modes in these anisotropic models show several significant effects which do not exist when the solid is isotropic or transversely isotropic with its symmetry axis parallel to the borehole:

1. The phase velocities for the quasi-pseudo-Rayleigh, both quasi-flexural, and both quasi-screw waves do not exceed the phase velocity of the slowest qS-wave. (The phase velocities of the leaky modes, which were not investigated in this paper, will exceed this threshold.)

2. The two quasi-flexural waves have different phase and group velocities; the differences are greatest at low frequencies and diminish as the frequency increases. The two quasi-screw waves behave similarly.

3. The greater the difference between the the phase velocities of the qS-waves, the greater the difference between the phase velocities of the quasi-flexural waves at all frequencies. The two quasi-screw waves behave similarly.

4. Near the limiting qS-wave velocity, the difference between the phase velocities for the two quasi-flexural waves is greater than that for the two quasi-screw waves.

5. For the slow quasi-flexural wave, the particle displacements in the plane perpendicular to the borehole, when viewed together, are aligned with the polarization

of the slow qS-wave.

6. For the fast quasi-flexural wave, the particle displacements in the plane perpendicular to the borehole, when viewed together, are aligned with the polarization of the fast qS-wave.

7. For the slow quasi-screw wave, the particle displacements in the plane perpendicular to the borehole, when viewed together, are aligned along two mutually perpendicular directions which are rotated 45° with respect to the polarizations of both qS-waves.

8. For the fast quasi-screw wave, the particle displacements in the plane perpendicular to the borehole, when viewed together, are aligned along two mutually perpendicular directions which are parallel with the polarizations of both qS-waves.

(In this list, the qS-waves refer to the plane waves whose wavenumber vectors are parallel to the borehole.) Despite these significant effects, the general characteristics of the phase velocities, group velocities, and displacements are similar (but not identical) to those that would exist if the solid were isotropic or transversely isotropic with its symmetry axis parallel to the borehole. This result is expected because the solid is only slightly anisotropic.

ACKNOWLEDGEMENTS

This work was supported by the Full Waveform Acoustic Logging Consortium at M.I.T. K. J. Ellefsen was partially supported by the Phillips Petroleum Fellowship.

REFERENCES

Aki, K. and P. G. Richards, *Quantitative Seismology,* W. H. Freeman & Co., 1980.

Auld, B. A., *Acoustic Fields and Waves in Solids,* vol. 1, John Wiley & Sons, Inc., 1973.

Backus, G. E., Long-wave anisotropy produced by horizontal layering, *J. Geophys. Res., 67,* 4427–4400, 1962.

Bathe, K., *Finite Element Procedures in Engineering Analysis,* Prentice-Hall, Inc., 1982.

Bettess, P., Infinite elements, *Int. J. Numer. Meth. Engng., 11,* 53–64, 1977.

Buland, R., and F. Gilbert, Computation of the free oscillations of the earth, *J. Comp. Phys., 54,* 95–114, 1984.

Bullen, K. E., *An Introduction to the Theory of Seismology,* Cambridge University Press, 1963.

Carrier, G. F., and C. E. Pearson, *Partial Differential Equations,* Academic Press Inc., 1976.

Chan, A. K., and L. Tsang, Propagation of acoustic waves in a fluid-filled borehole surrounded by a concentrically layered transversely isotropic formation, *J. Acoust. Soc. Am., 74,* 1605–1616, 1983.

Chen, H. C. and R. L. Taylor, Solution of eigenproblems for damped structural systems by the Lanczos algorithm, *Comput. Struct., 30,* 151–161, 1988.

Crampin, S., Effective elastic constants for wave propagation through cracked solids, *Geophys. J. Roy. Astron. Soc., 76,* 135–145, 1984.

Everstine, G. C., A symmetric potential formulation for fluid-structure interaction, *J. Sound Vib., 79,* 157–160, 1981.

Goldstein, H., *Classical Mechanics,* Addison-Wesley Publishing Co., 1980.

Hamdi, M. A., and Y. Ousset, A displacement method for the analysis of vibrations of coupled fluid-structure systems, *Int. J. Numer. Meth. Engng., 13,* 139–150, 1978.

Huang, K. H., and S. B. Dong, Propagating waves and edge vibrations in anisotropic composite cylinders, *J. Sound Vib., 96,* 363–379, 1984.

Kausel, E., Wave propagation in anisotropic layered media, *Int. J. Numer. Meth. Engng., 23,* 1567–1578, 1986.

Kausel, E., and J. M. Roësset, Stiffness matrices for layered soils, *Bull. Seis. Soc. Am., 71,* 1743–1761, 1981.

Kennett, B. L. N., *Seismic Wave Propagation in Stratified Media,* Cambridge University Press, 1983.

Lamb, H., *Hydrodynamics,* Cambridge University Press, 1879.

Lanczos, C., *The Variational Principles of Mechanics,* University of Toronto Press, 1970.

Lathi, B. P., *Signals, Systems and Communication,* John Wiley & Sons, Inc., 1965.

Leveille, J. P. and A. J. Seriff, Borehole wave particle motion in anisotropic formations, *J. Geophys. Res., 94,* 7183–7188, 1989.

Lysmer, J., Lumped mass method for Rayleigh waves, *Bull. Seis. Soc. Am., 60,* 89–104, 1970.

Lysmer, J., and L. A. Drake, A finite element method for seismology, in *Methods in Computational Physics; Seismology: Surface Waves and Earth Oscillations,* edited by B. A. Bolt, pp. 181–216, Academic Press Inc., 1982.

Mathews, J., and R. L. Walker, *Mathematical Methods of Physics,* Benjamin-Cummings Publishing Co., 1970.

Miklowitz, J., *The Theory of Elastic Waves and Waveguides,* North-Holland Publishing Co., 1978.

Nelson, R. B., Natural vibrations of laminated orthotropic spheres, *Int. J. Solids Structures, 9,* 305–311, 1973.

Nelson, R. B., S. B. Dong, and R. D. Kalra, Vibrations and waves in laminated orthotropic circular cylinders, *J. Sound Vib., 18,* 429–444, 1971.

Nicoletis, L. M., A. Bamberger, J. A. Quiblier, P. Joly, and M. Kern, Hole geometry and anisotropic effects on tube-wave propagation: A quasi-static study, *Geophysics, 55,* 167–175, 1990.

Olsen, L. G., and K. Bathe, Analysis of fluid-structure interactions: a direct symmetric coupled formulation based on the fluid velocity potential, *Comput. Struct., 21,* 21–32, 1985.

Redwood, M., *Mechanical Waveguides,* Pergamon Press Ltd., 1960.

Schmitt, D. P., Acoustic multipole logging in transversely isotropic poroelastic formations, *J. Acoust. Soc. Am., 86,* 2397–2421, 1989.

Thill, R. E., T. R. Bur, and R. C. Steckley, Velocity anisotropy in dry and saturated rock spheres and its relation to rock fabric, *Int. J. Rock Mech. Min. Sci. and Geomech., 10,* 535–557, 1973.

Thomsen, L., Weak elastic anisotropy, *Geophysics, 51,* 1954–1966, 1986.

Thurston, R. N., Elastic waves in rods and clad rods, *J. Acoust. Soc. Am., 64,* 1–37, 1978.

Tongtaow, C., Transient response of an acoustic logging tool in transversely isotropic media, Master's thesis, Colorado School of Mines, 1980.

Tongtaow, C., Wave propagation along a cylindrical borehole in a transversely isotropic formation, PhD thesis, Colorado School of Mines, 1982.

White, J. E. and F. A. Angona, Elastic wave velocities in laminated media, *J. Acoust. Soc. Am., 27,* 310–317, 1955.

White, J. E, and C. Tongtaow, Cylindrical waves in transversely isotropic media, *J. Acoust. Soc. Am., 70,* 1147–1155, 1981.

Wiggins, R. A., A fast, new computational algorithm for free oscillations and surface waves, *Geophys. J. Roy. Astron. Soc., 47,* 135–150, 1976.

Winterstein, D. F., Anisotropy effects in *P*-wave and *SH*-wave stacking velocities contain information on lithology, *Geophysics, 51,* 661–672, 1986.

Zoback, M. D., D. Moos, and L. Mastin, Well bore breakouts and in situ stress, *J. Geophys. Res., 90,* 5523–5530, 1985.

Region	Meaning	Variable
fluid	volume	V_1
	density	ρ_1
	incompressibility	λ_1
	velocity potential	ϕ
	dilatation	Θ
solid	volume	V_2
	density	ρ_2
	stiffness matrix	$\mathbf{C}$
	strain vector	$\mathbf{E}$
fluid-solid interface	surface	Σ
	normal vector	$\mathbf{n}$
	normal displacement	u_N
general	cylindrical coordinates	r, θ, z
	Cartesian coordinates	x, y, z
	displacement	$\mathbf{u}$
	time	t
	wavenumber for z direction	k_z
	frequency	ω
	phase velocity	v
	group velocity	U_G
	pressure	p
	borehole radius	R
	surface area	S
	volume	V
	Lagrangian energy	L

Table 1: Variables needed to formulate the variational equations and other miscellaneous variables.

Region	Meaning	Variable
fluid (element m)	interpolating functions	$h_i^{(m)}(x,y)$ or $\mathbf{h}^{(m)}(x,y)$
	velocity potential at nodes	$\Phi_i^{(m)}(k_z,t)$ or $\mathbf{\Phi}^{(m)}(k_z,t)$
	stiffness matrices	$\mathbf{K}_{0F}^{(m)}$, $\mathbf{K}_{2F}^{(m)}$
	mass matrix	$\mathbf{M}_F^{(m)}$
fluid (all elements)	velocity potential	$\bar{\mathbf{\Phi}}(k_z,t)$
	stiffness matrices	$\mathbf{K}_{0F}$, $\mathbf{K}_{2F}$
	mass matrix	$\mathbf{M}_F$
solid (element n)	interpolating functions	$h_i^{(n)}(x,y)$ or $\mathbf{H}^{(n)}(x,y)$
	strain matrix for x and y directions	$\mathbf{B}_0^{(n)}(x,y)$
	strain matrix for z directions	$\mathbf{B}_1^{(n)}(x,y)$
	displacement at nodes	$U_{ix}^{(n)}(k_z,t)$, $U_{iy}^{(n)}(k_z,t)$, $U_{iz}^{(n)}(k_z,t)$ or $\mathbf{U}^{(n)}(k_z,t)$
	stiffness matrices	$\mathbf{K}_{0S}^{(n)}$, $\mathbf{K}_{1S}^{(n)}$, $\mathbf{K}_{2S}^{(n)}$
	mass matrix	$\mathbf{M}_S^{(n)}$
solid (all elements)	displacement	$\mathbf{U}(k_z,t)$
	stiffness matrices	$\mathbf{K}_{0S}$, $\mathbf{K}_{1S}$, $\mathbf{K}_{2S}$
	mass matrix	$\mathbf{M}_S$
fluid-solid interface (element q)	distance along Σ	l
	angle between $\mathbf{n}$ and Σ at node i	$\theta_i^{(q)}$
	interpolating functions	$h_{Ii}^{(q)}(l)$
	interpolating matrix for fluid	$\mathbf{h}_I^{(q)}(l)$
	interpolating matrix for solid	$\mathbf{H}_I^{(q)}(l)$
	coupling matrix	$\mathbf{F}^{(q)}$
fluid-solid interface (all elements)	coupling matrix	$\mathbf{F}$
general	number of fluid elements	M
	number of solid elements	N
	number of interface elements	Q
	vector and matrices in wave equation	$\mathbf{Y}$, $\mathbf{V}$, $\mathbf{A}_0$, $\mathbf{A}_1$, $\mathbf{A}_2$, $\mathbf{A}_0'$, $\mathbf{D}_1$, $\mathbf{D}_2$

Table 2: Additional variables needed for the finite element solution to the variational equation.

Quantity	Value
c_{11}	3.79×10^{10} Pa
c_{44}	1.51×10^{10} Pa
ρ_2	2140 kg/m^3
λ_1	0.225×10^{10} Pa
ρ_1	1000. kg/m^3
R	0.1016 m

Table 3: Properties of the isotropic model with a fast formation. The properties of the solid are like those for the Berea sandstone (Thomsen, 1986).

Quantity	Value
c_{11}	0.998×10^{10} Pa
c_{44}	0.117×10^{10} Pa
ρ_2	2250kg/m^3
λ_1	0.225×10^{10} Pa
ρ_1	1000. kg/m^3
R	0.1016 m

Table 4: Properties of the isotropic model with a slow formation.

Quantity	Value
c_{11}	7.23×10^{10} Pa
c_{13}	2.06×10^{10} Pa
c_{33}	6.50×10^{10} Pa
c_{44}	2.21×10^{10} Pa
c_{66}	2.51×10^{10} Pa
ρ_2	2500 kg/m^3
λ_1	0.225×10^{10} Pa
ρ_1	1000. kg/m^3
R	0.1016 m

Table 5: Properties of the transversely isotropic model. For this list of elastic constants, the symmetry axis is parallel to the z axis. The properties of the solid are like those for the Mesaverde shale (5496.5) (Thomsen, 1986).

Quantity	Value
c_{11}	9.78×10^{10} Pa
c_{12}	1.95×10^{10} Pa
c_{13}	3.23×10^{10} Pa
c_{22}	9.09×10^{10} Pa
c_{23}	1.86×10^{10} Pa
c_{33}	8.17×10^{10} Pa
c_{44}	2.44×10^{10} Pa
c_{55}	2.00×10^{10} Pa
c_{66}	3.18×10^{10} Pa
ρ_2	2800 kg/m^3
λ_1	0.225×10^{10} Pa
ρ_1	1000. kg/m^3
R	0.1016 m

Table 6: Properties of the orthorhombic model. The symmetry planes for the orthorhombic solid are parallel to the coordinate planes. The properties of the solid were measured by J. Mendelson (1989, oral communication).

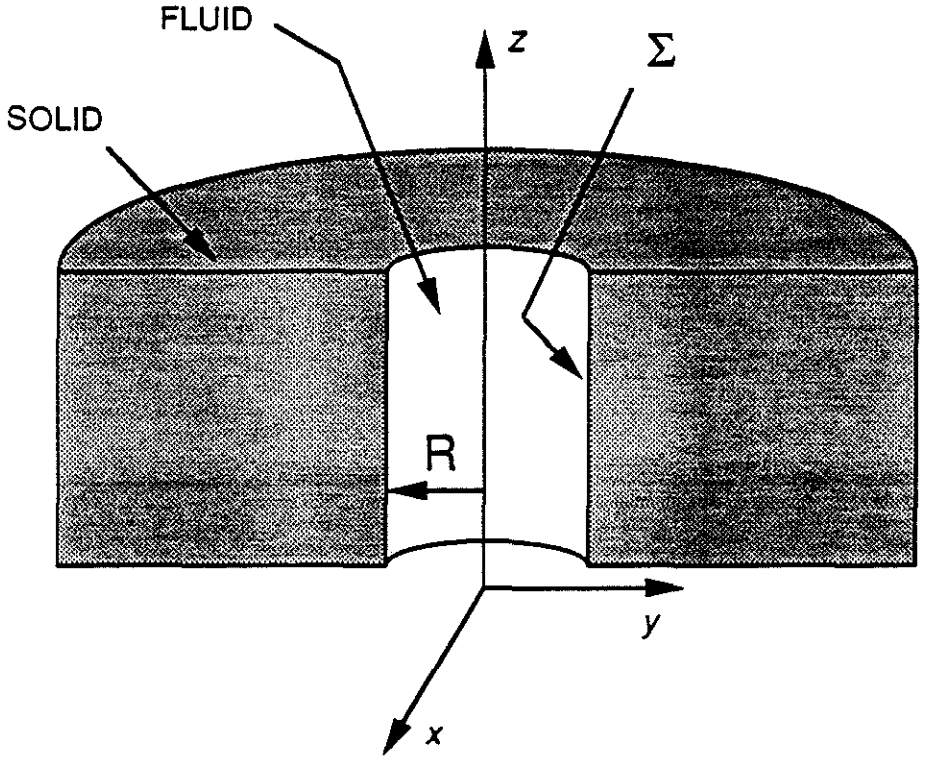

Figure 1: Cutaway view of the mathematical model.

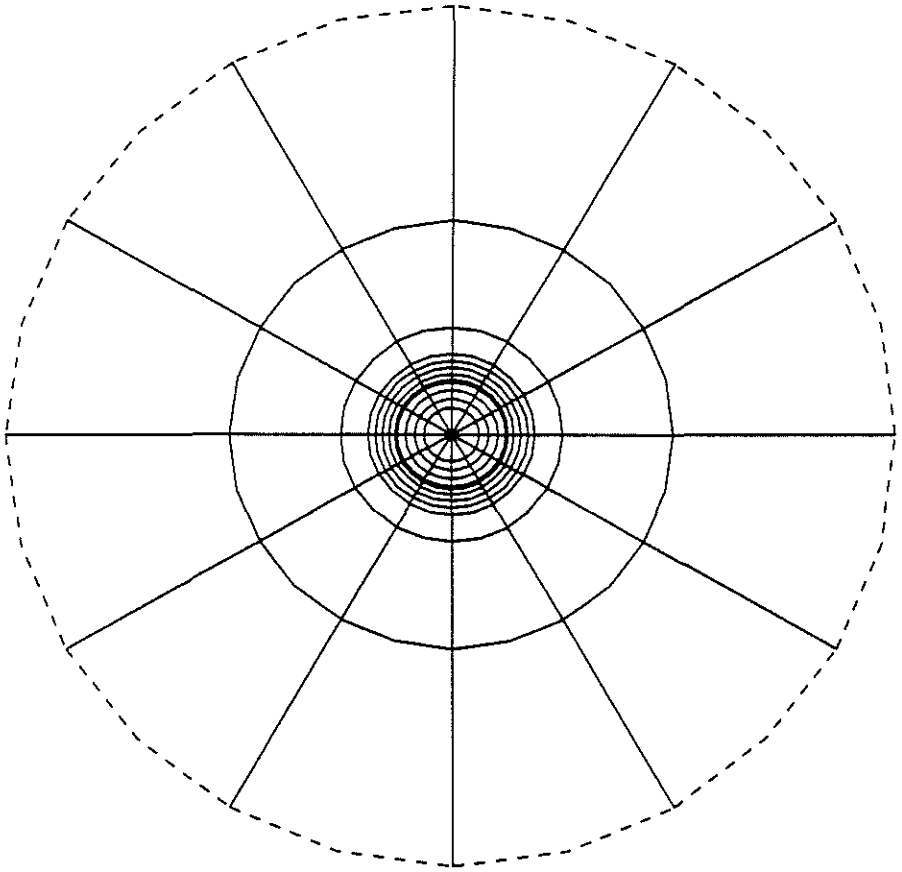

Figure 2: Finite element mesh. The location of the fluid-solid interface is shown by the dark line. The outermost elements actually extend to infinity which is symbolized by the dashed line.

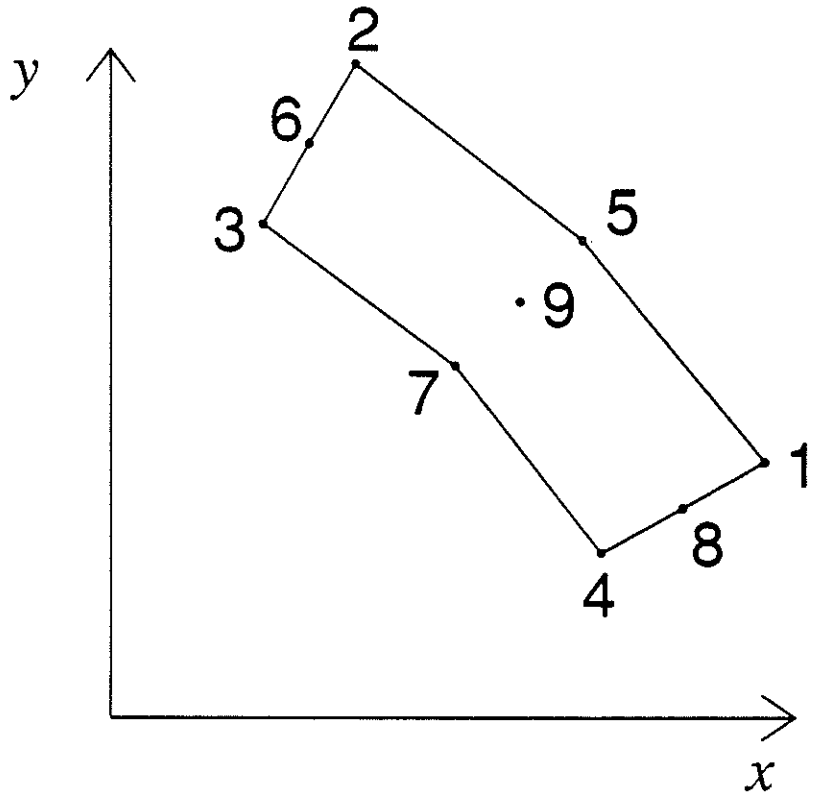

Figure 3: A two-dimensional element with nine nodes. This type of element is used in the fluid and solid regions.

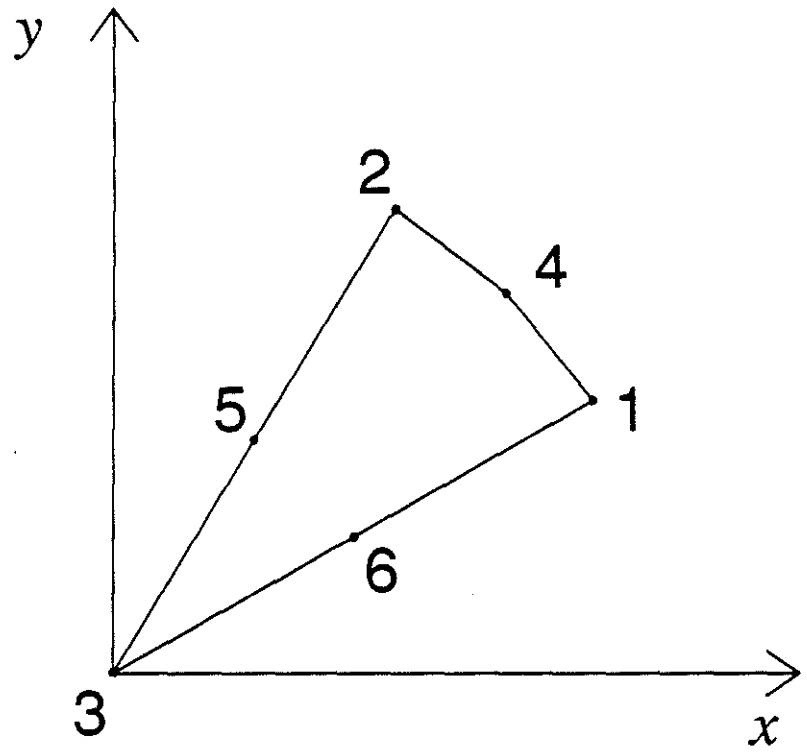

Figure 4: A two-dimensional element with six nodes. This type of element is used only in the center of the mesh.

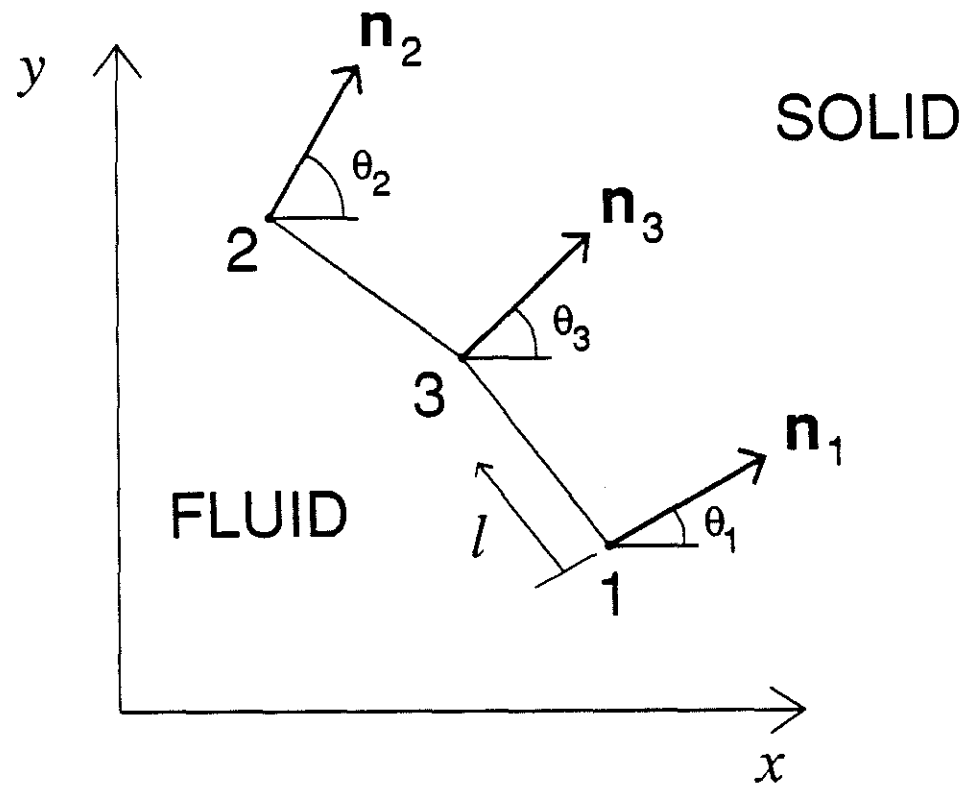

Figure 5: An interface element. This element has three nodes, and distances along the element are specified by l.

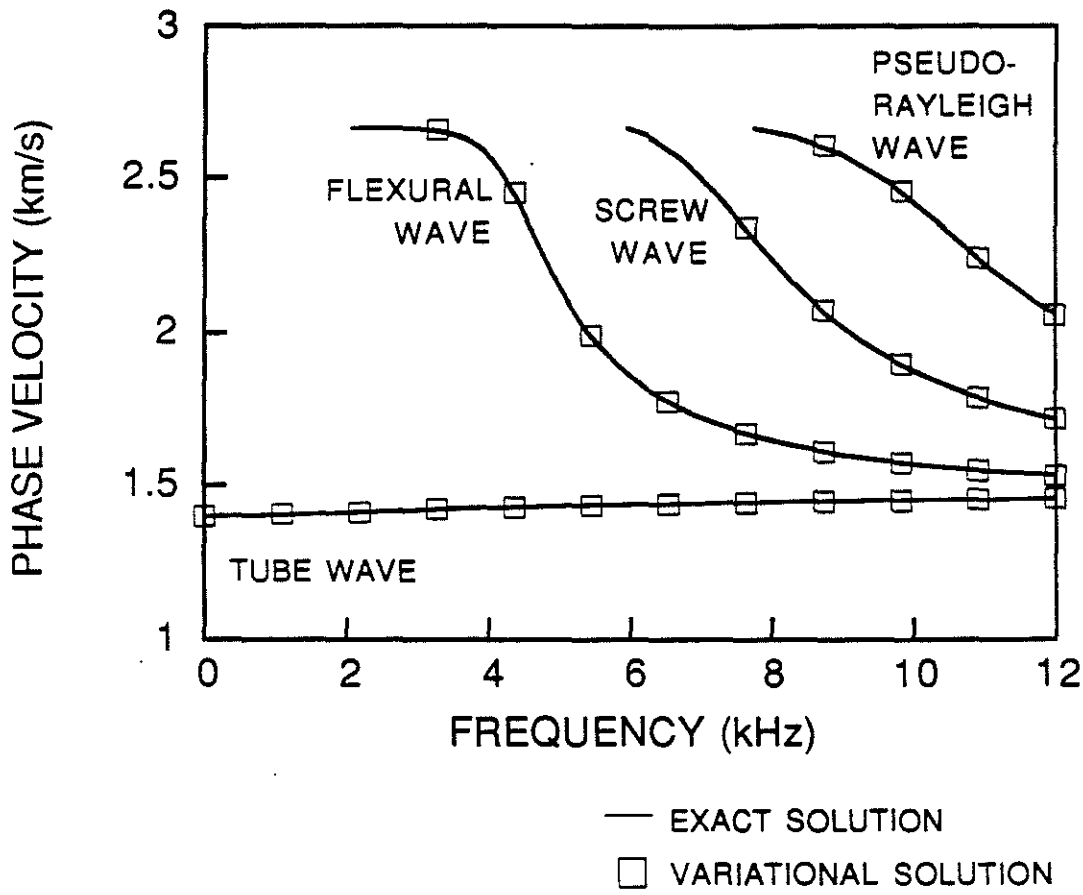

Figure 6: Accuracy of the phase velocities calculated with the variational method. The model has an isotropic, fast formation (Table 3).

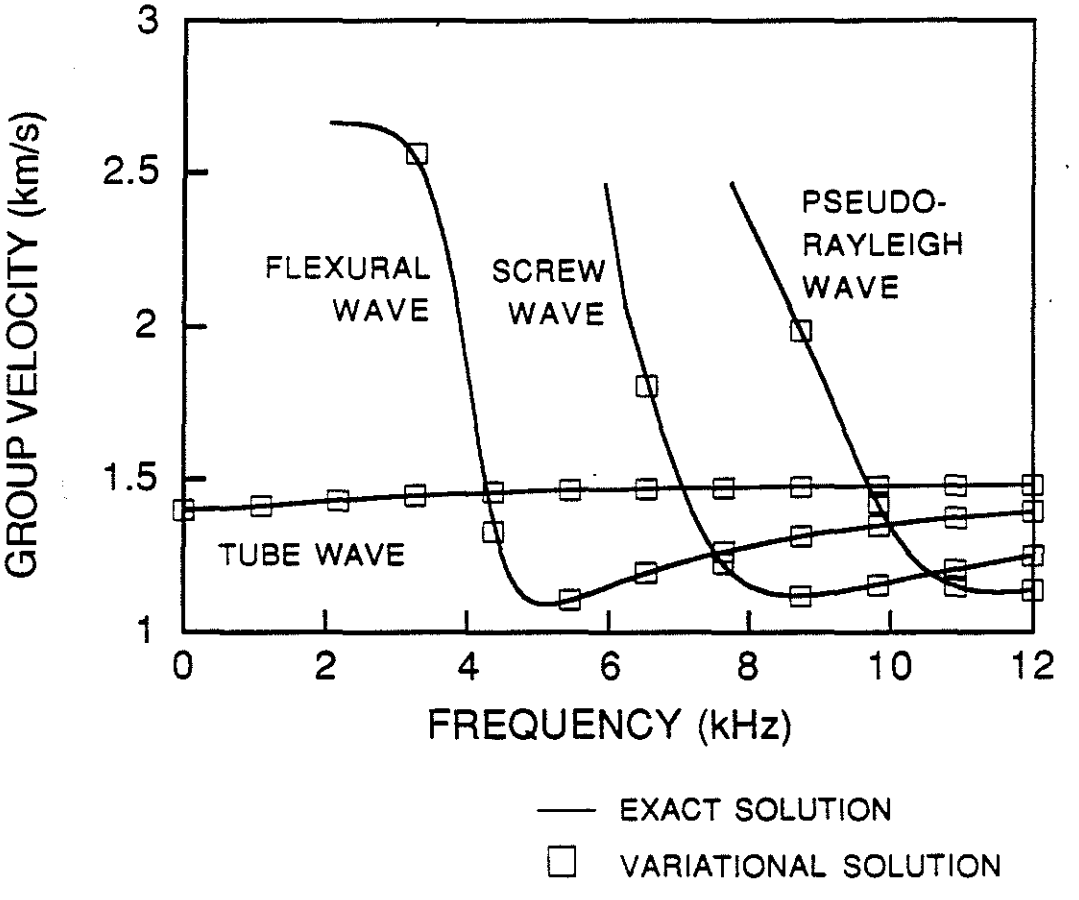

Figure 7: Accuracy of the group velocities calculated with the variational method. The model has an isotropic, fast formation (Table 3).

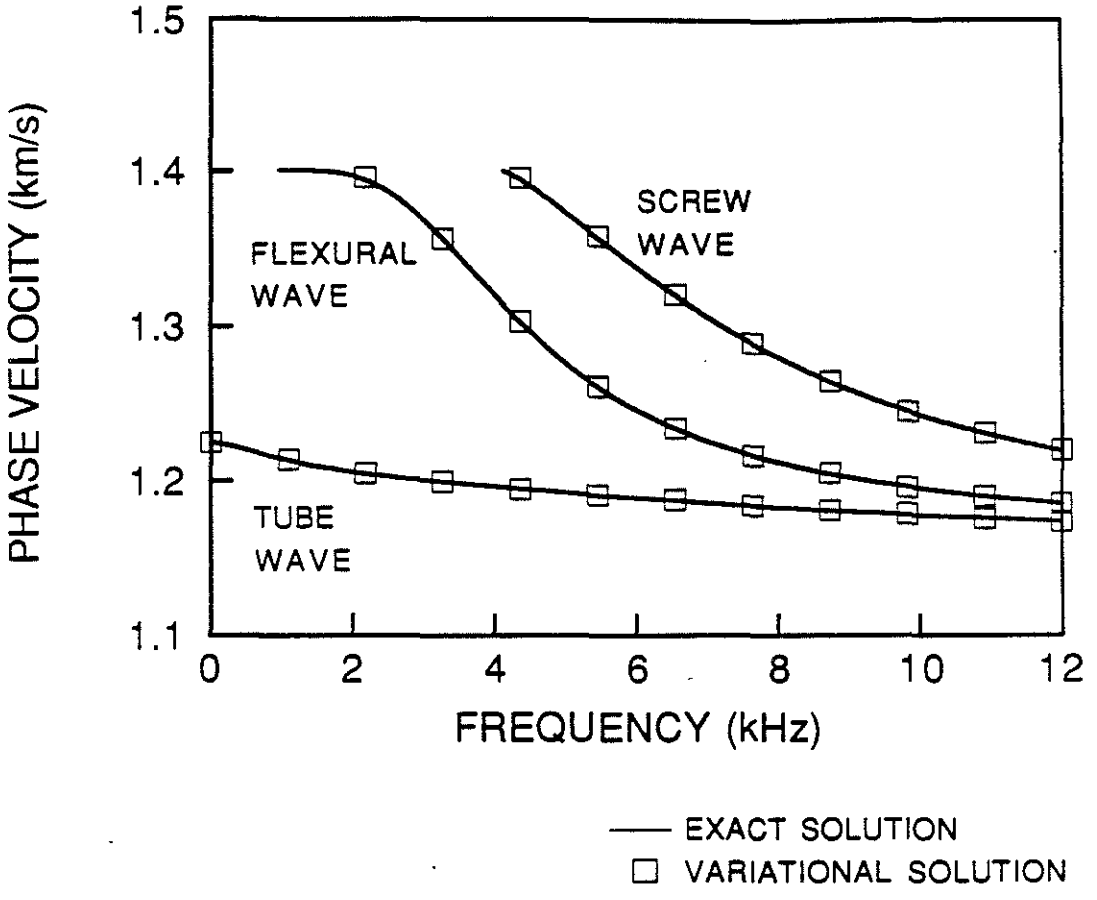

Figure 8: Accuracy of the phase velocities calculated with the variational method. The model has an isotropic, slow formation (Table 4).

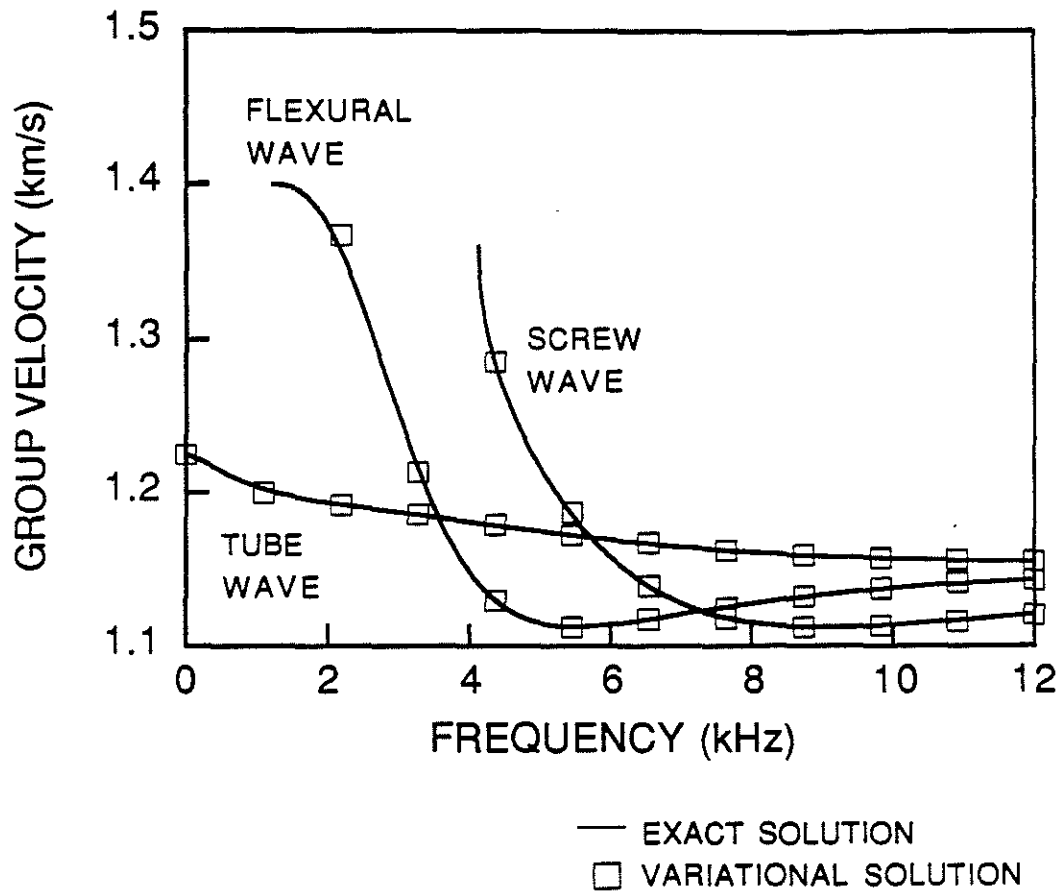

Figure 9: Accuracy of the group velocities calculated with the variational method. The model has an isotropic, slow formation (Table 4).

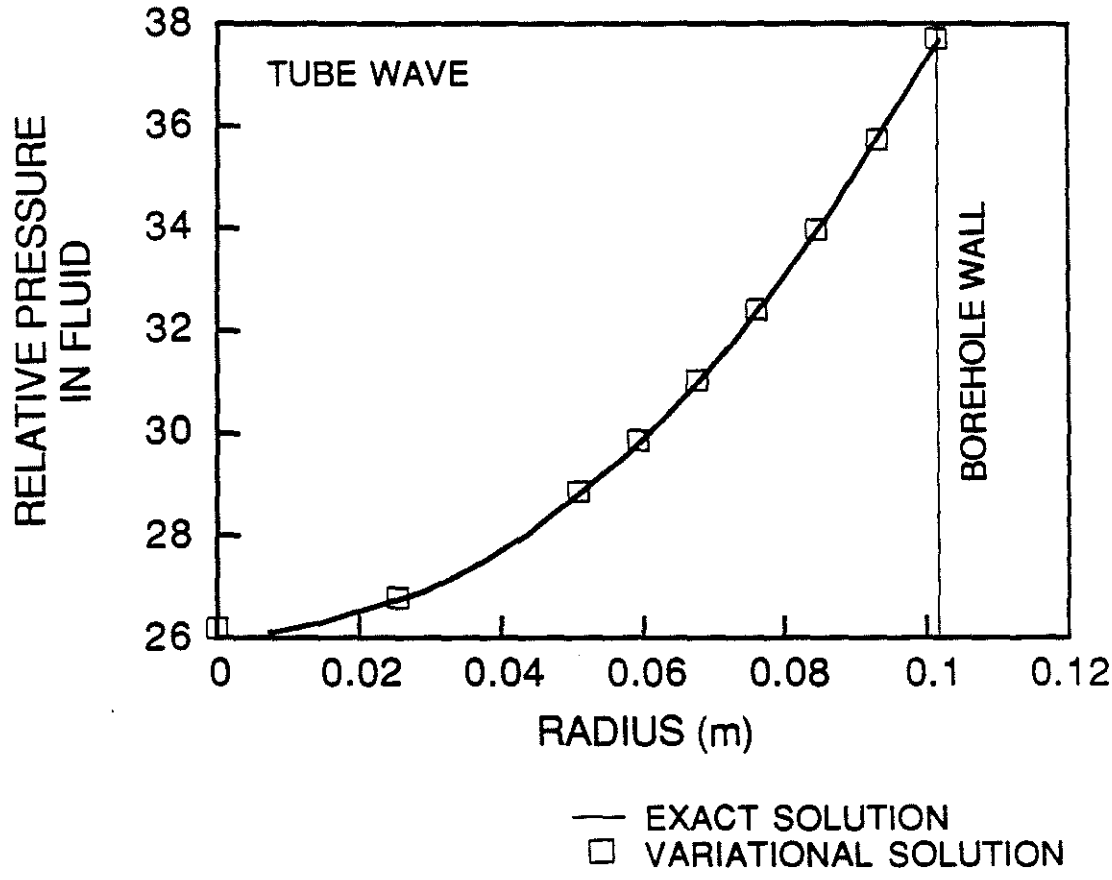

Figure 10: Accuracy of the pressures for the tube calculated with the variational method. The model has an isotropic, fast formation (Table 3).

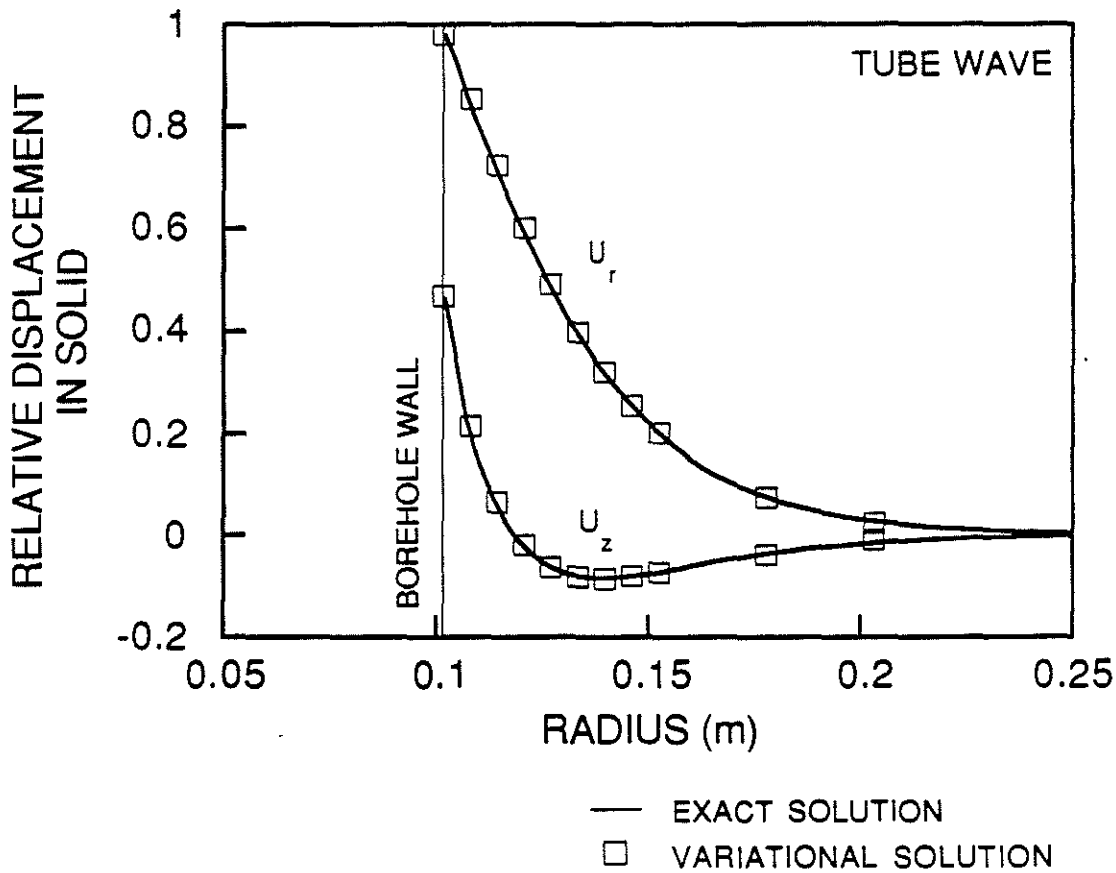

Figure 11: Accuracy of the displacements for the tube wave calculated with the variational method. The model has an isotropic, fast formation (Table 3).

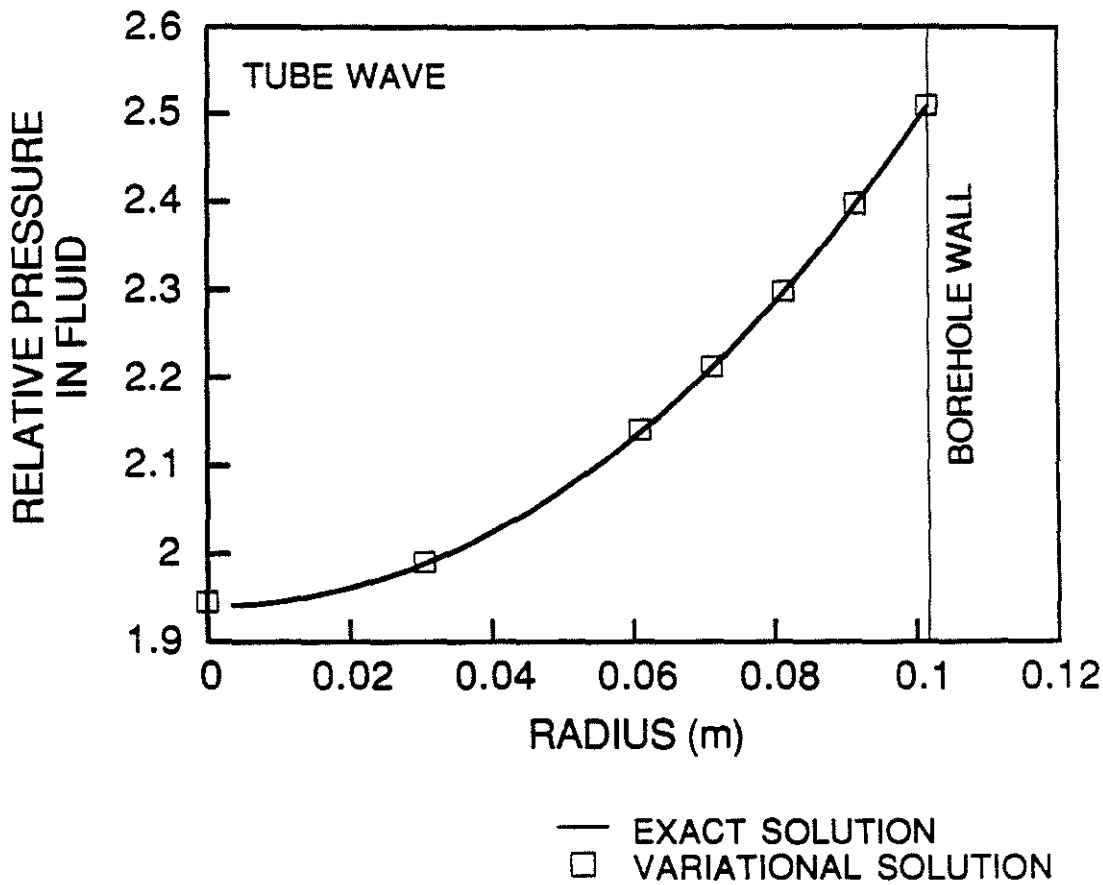

Figure 12: Accuracy of the pressures for the tube calculated with the variational method. The model has an isotropic, slow formation (Table 4).

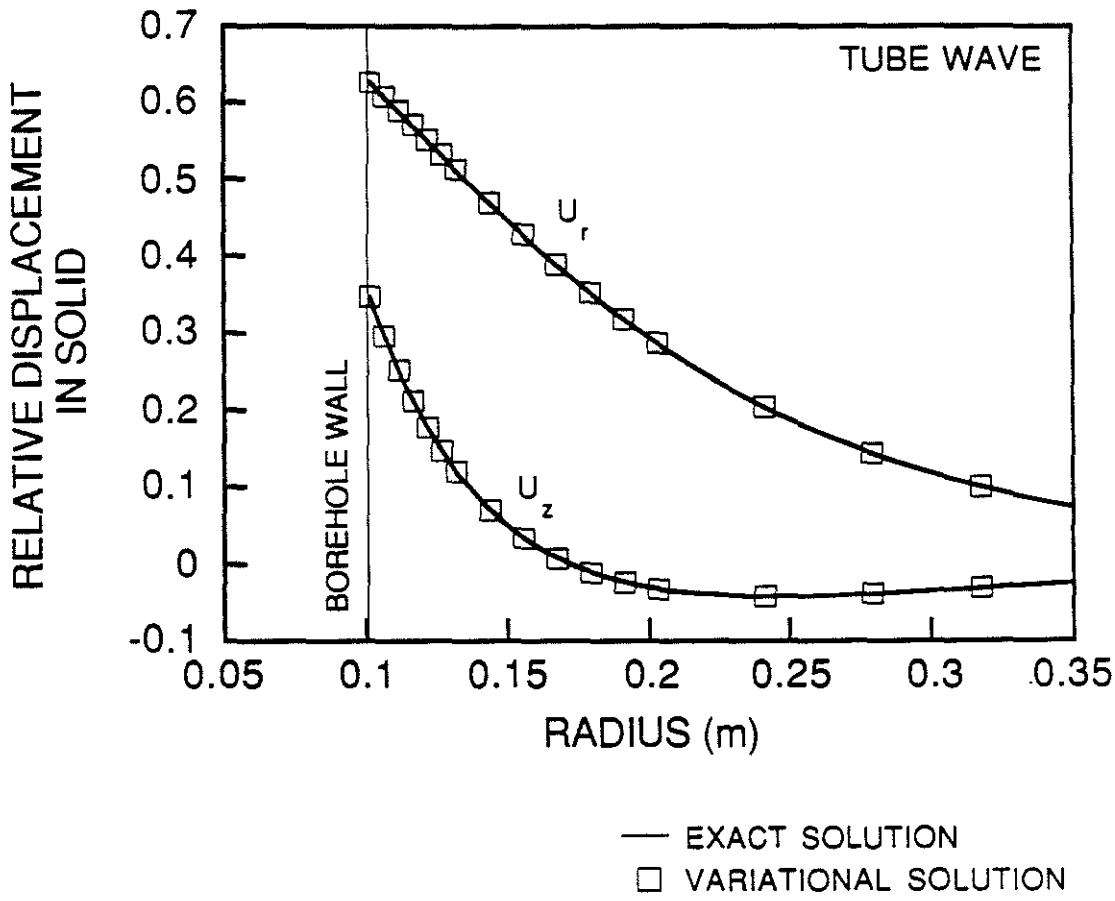

Figure 13: Accuracy of the displacements for the tube wave calculated with the variational method. The model has an isotropic, slow formation (Table 4).

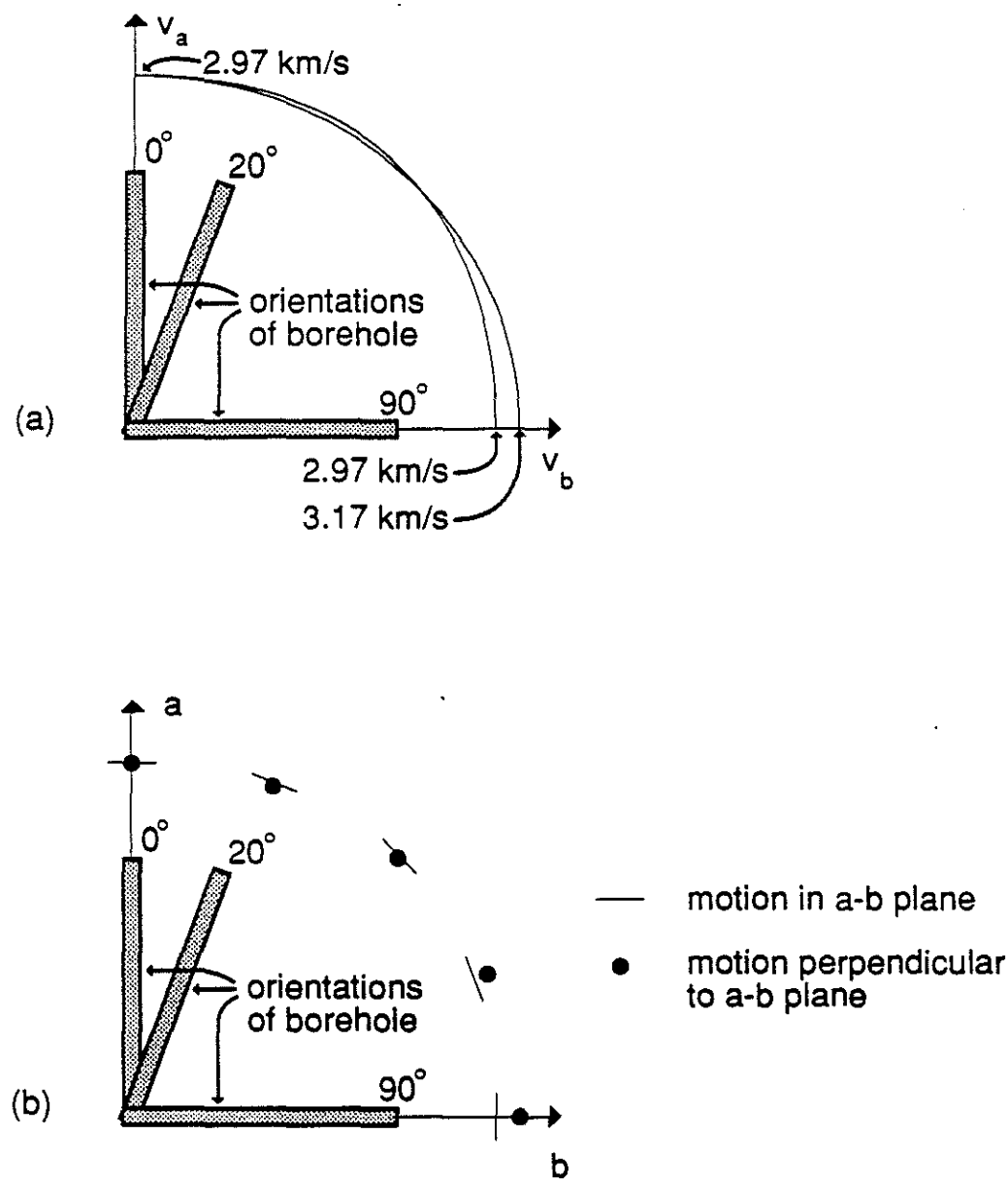

Figure 14: (a) Phase velocity surfaces and (b) polarizations for the qS-waves in the transversely isotropic model (Table 5). Axis a is parallel to the symmetry axis, and axis b is perpendicular to a and in an arbitrary direction.

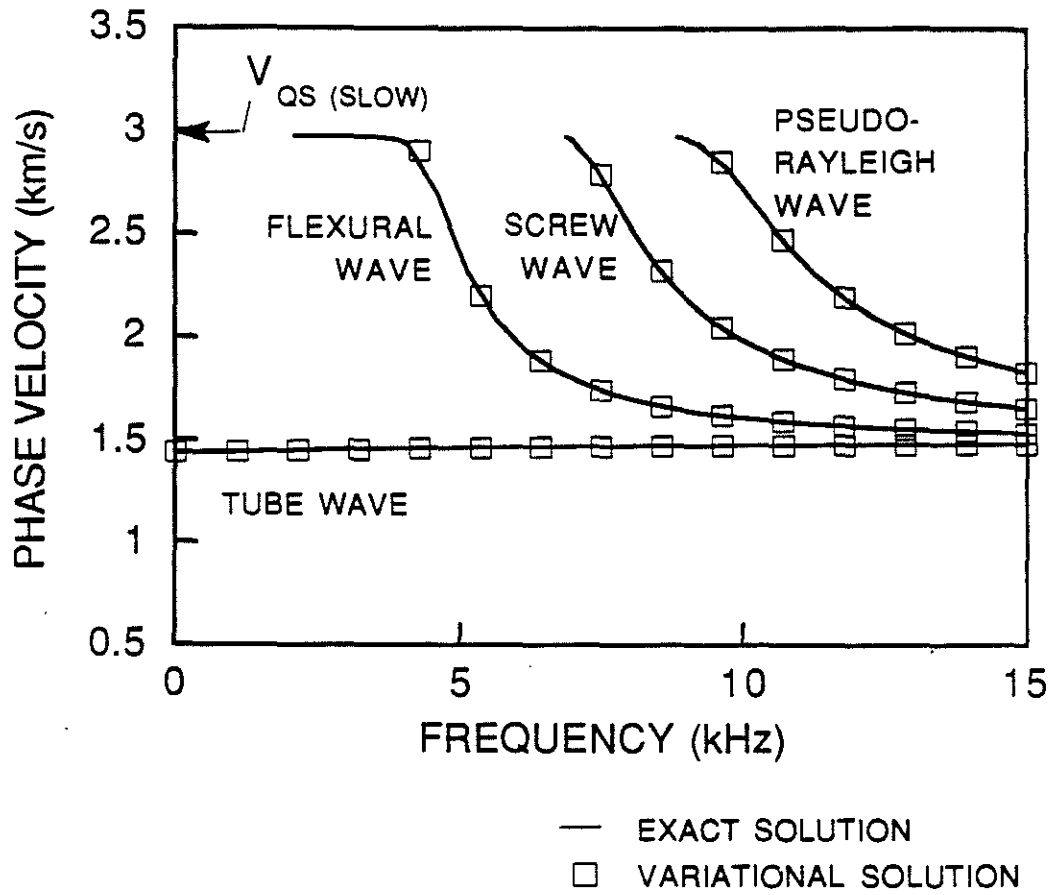

Figure 15: Phase velocities for the normal modes in the transversely isotropic model (Table 5) when the symmetry axis is parallel to the borehole.

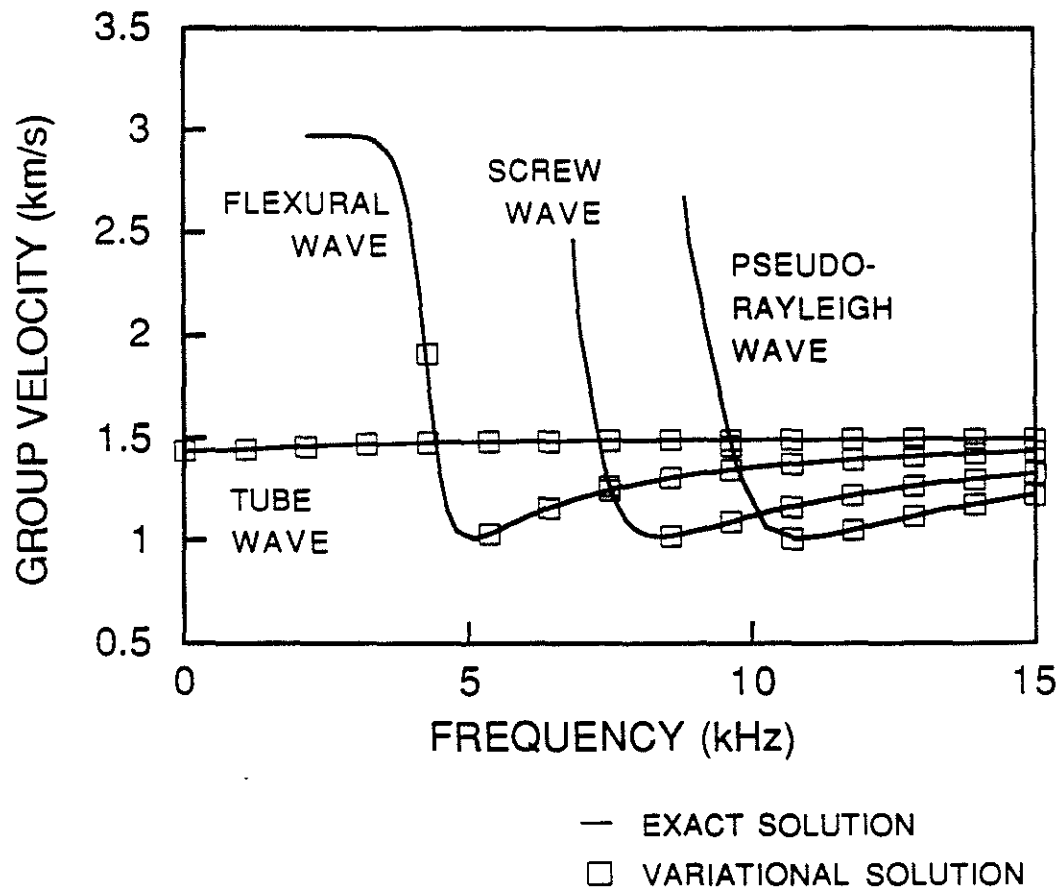

Figure 16: Group velocities for the normal modes in the transversely isotropic model (Table 5) when the symmetry axis is parallel to the borehole.

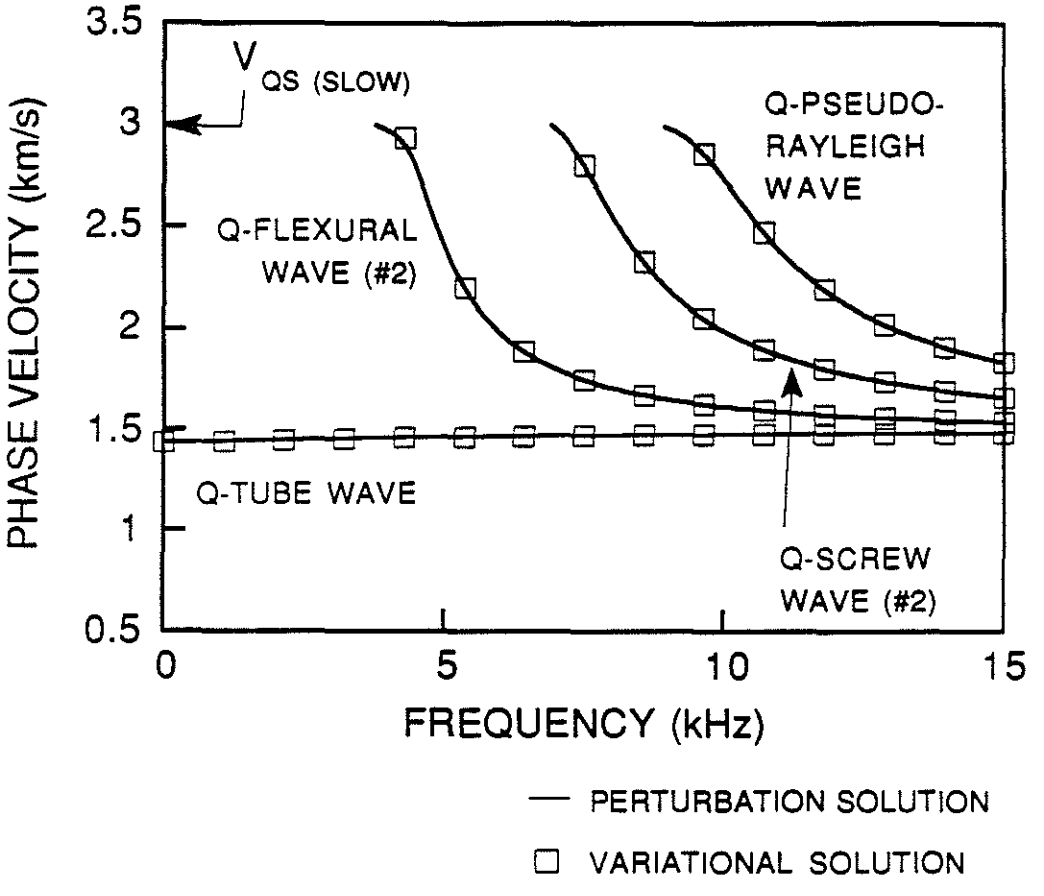

Figure 17: Phase velocities of the normal modes in the transversely isotropic model (Table 5) when its symmetry axis is tilted 20° with respect to the borehole. See also Figure 18.

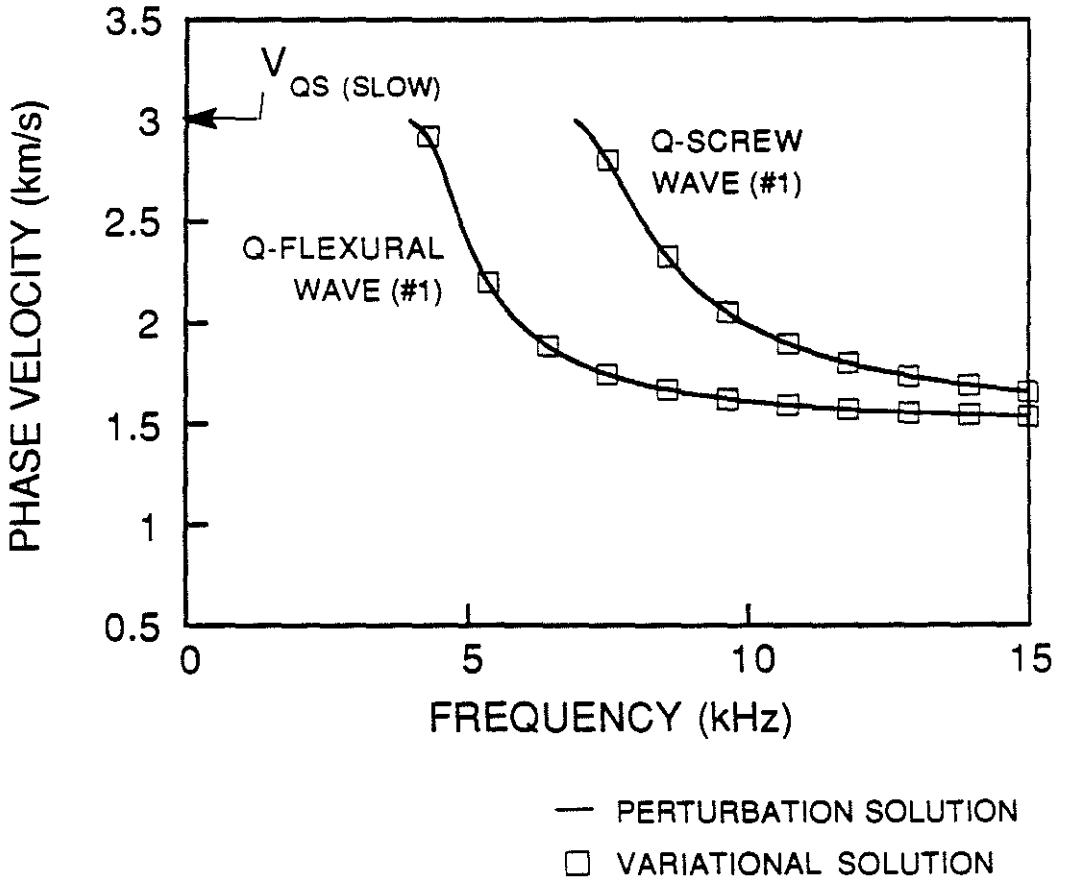

Figure 18: Phase velocities of the normal modes in the transversely isotropic model (Table 5) when its symmetry axis is tilted 20° with respect to the borehole. See also Figure 17.

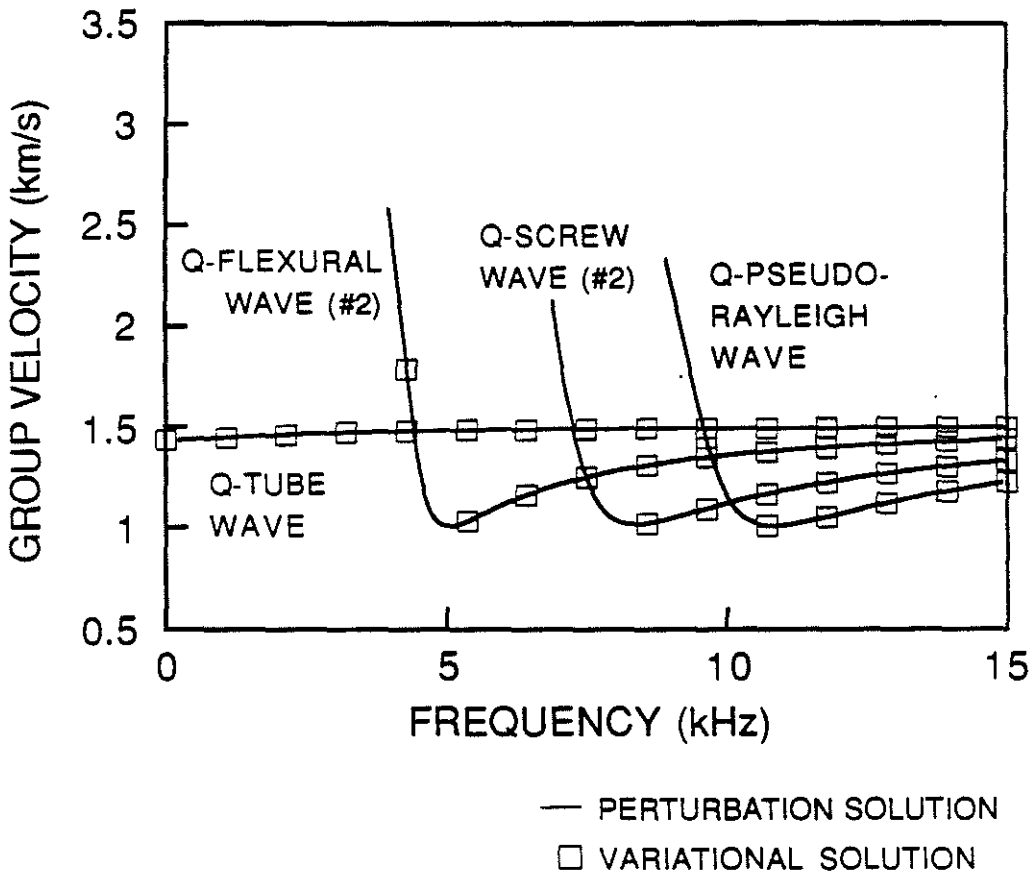

Figure 19: Group velocities of the normal modes in the transversely isotropic model (Table 5) when its symmetry axis is tilted 20° with respect to the borehole. See also Figure 20.

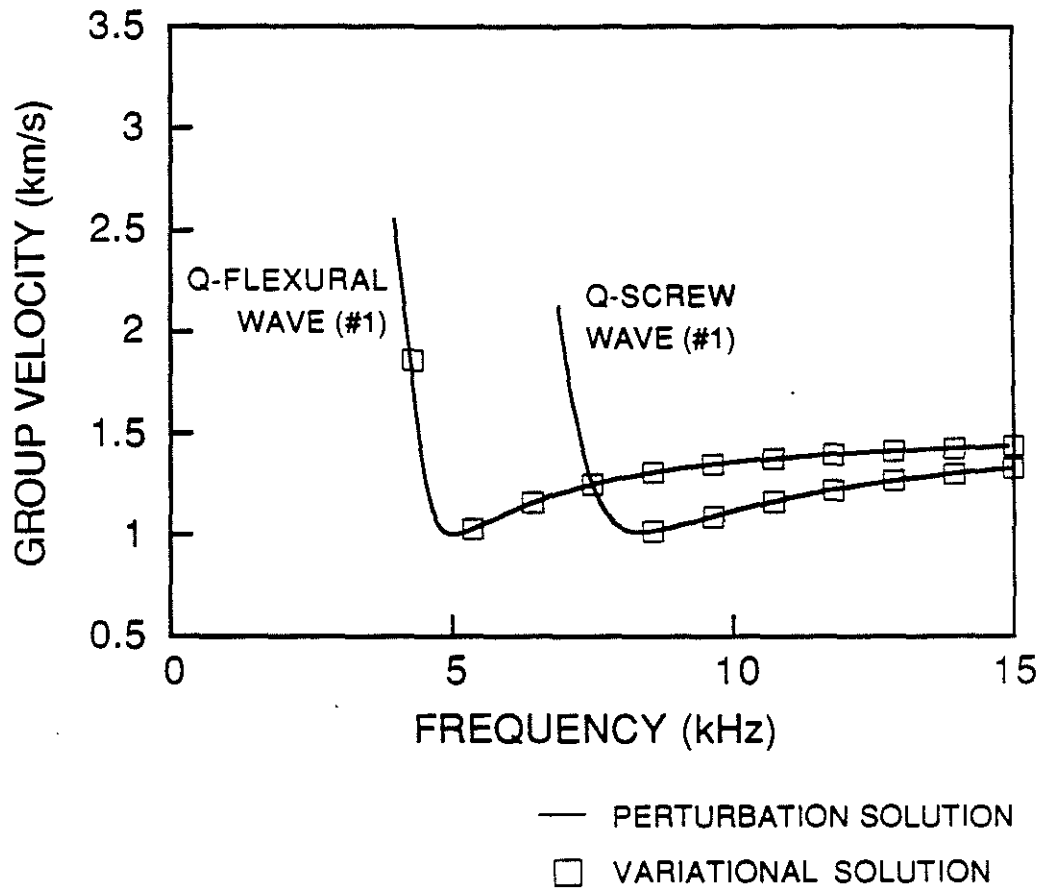

Figure 20: Group velocities of the normal modes in the transversely isotropic model (Table 5) when its symmetry axis is tilted 20° with respect to the borehole. See also Figure 19.

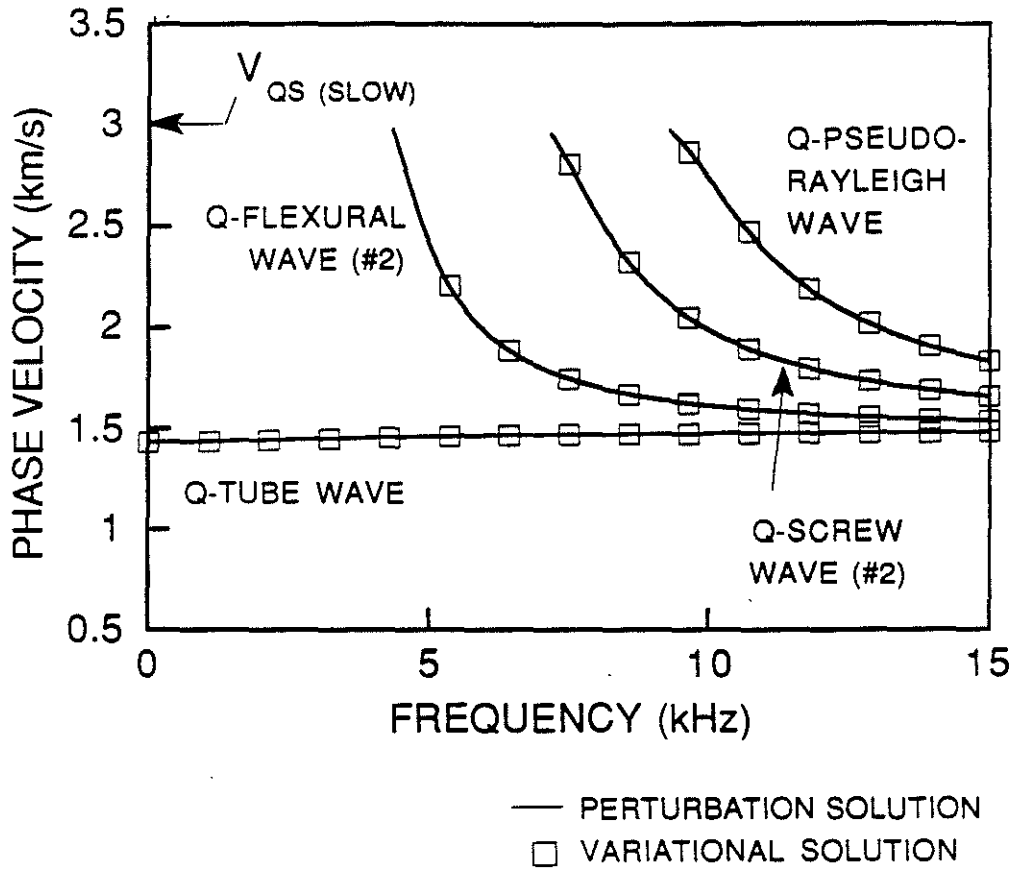

Figure 21: Phase velocities of the normal modes in the transversely isotropic model (Table 5) when its symmetry axis is tilted 90° with respect to the borehole. See also Figure 22.

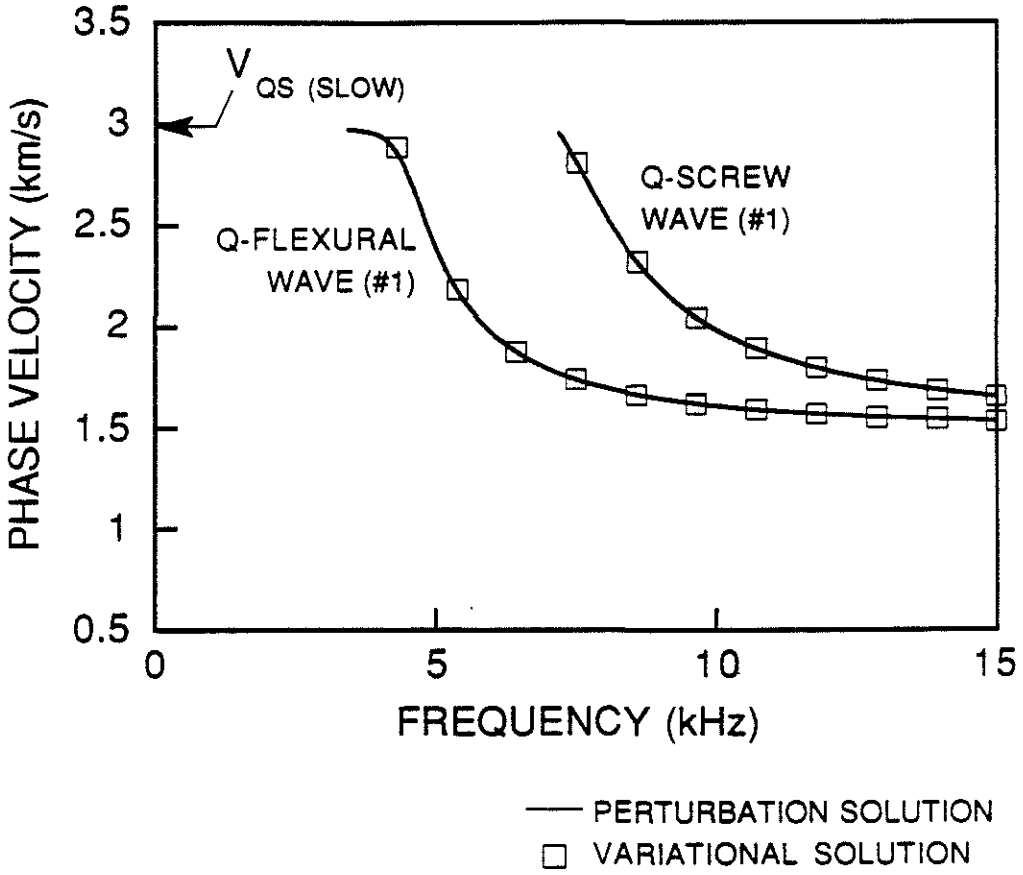

Figure 22: Phase velocities of the normal modes in the transversely isotropic model (Table 5) when its symmetry axis is tilted 90° with respect to the borehole. See also Figure 21.

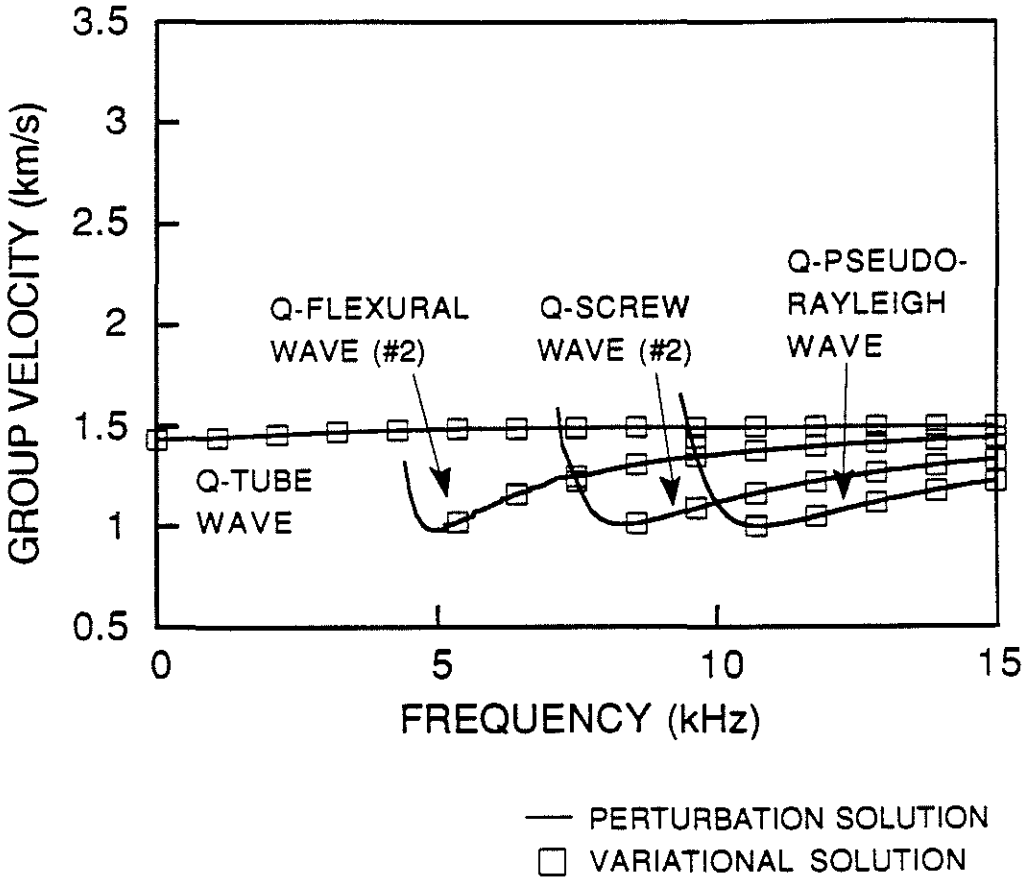

Figure 23: Group velocities of the normal modes in the transversely isotropic model (Table 5) when its symmetry axis is tilted 90° with respect to the borehole. See also Figure 24.

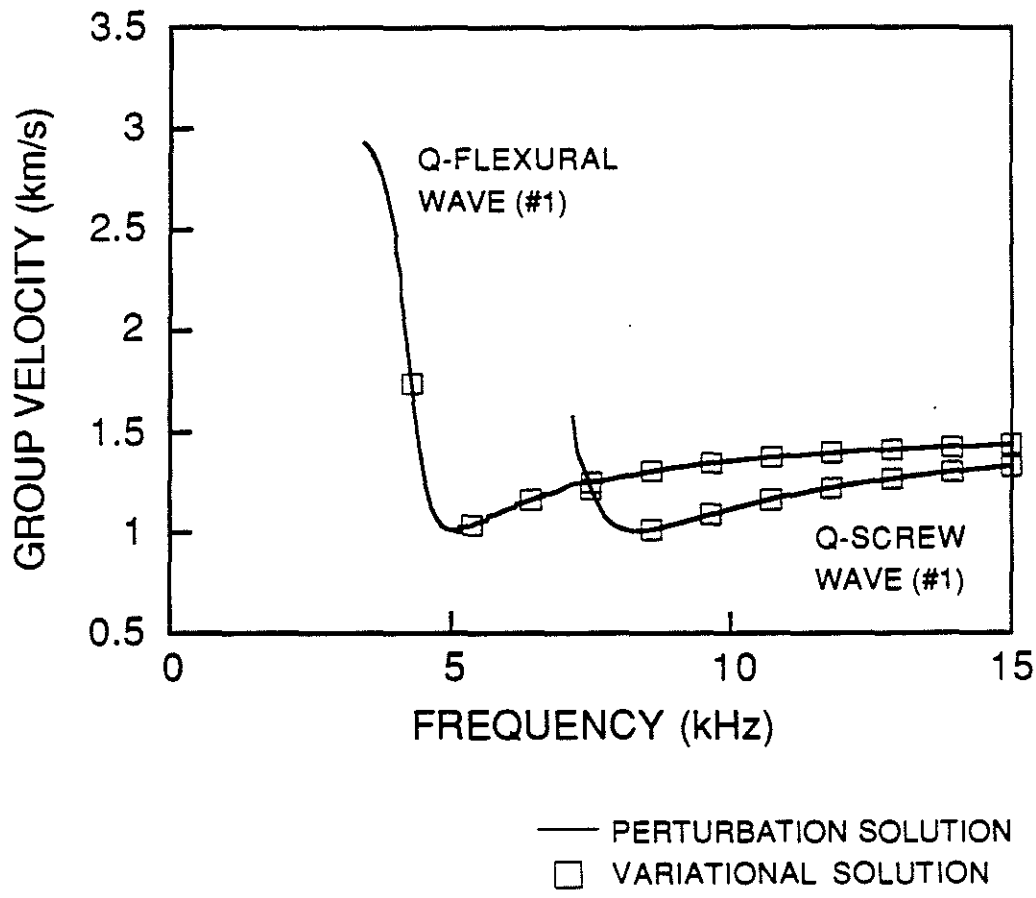

Figure 24: Group velocities of the normal modes in the transversely isotropic model (Table 5) when its symmetry axis is tilted 90° with respect to the borehole. See also Figure 23.

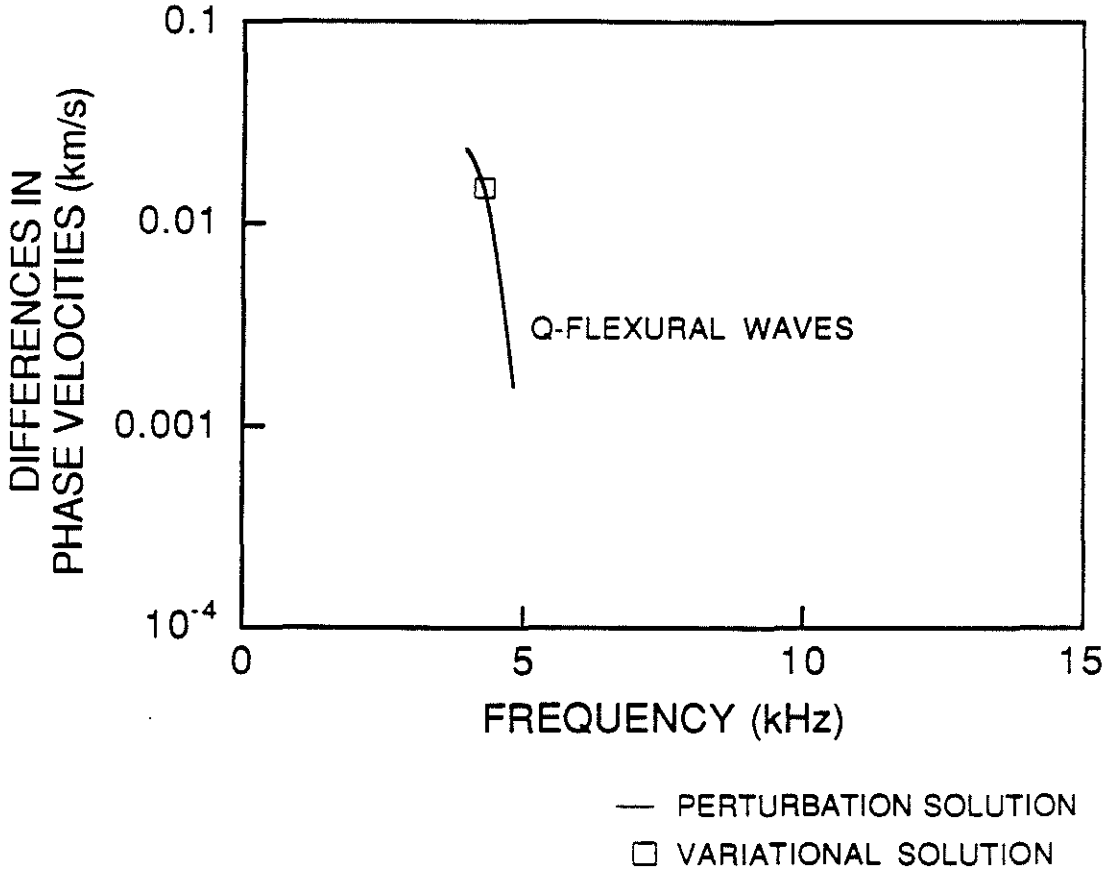

Figure 25: Differences between the phase velocities of the quasi-flexural waves (Figure 17 and 18) in the transversely isotropic model (Table 5) when its symmetry axis is tilted 20° with respect to the borehole. (When differences less than about 0.001 km/s become inaccurate, they are not plotted.)

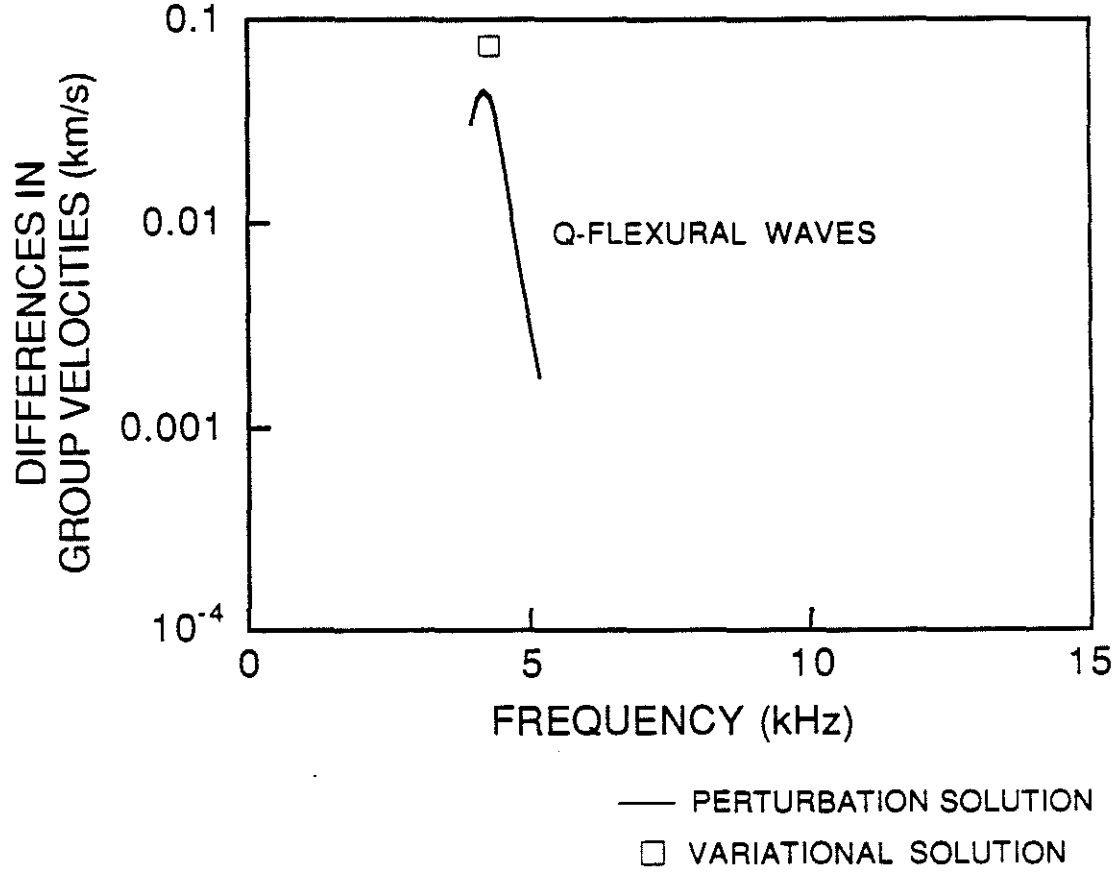

Figure 26: Differences between the group velocities of the quasi-flexural waves (Figure 19 and 20) in the transversely isotropic model (Table 5) when its symmetry axis is tilted 20° with respect to the borehole. (When differences less than about 0.001 km/s become inaccurate, they are not plotted.)

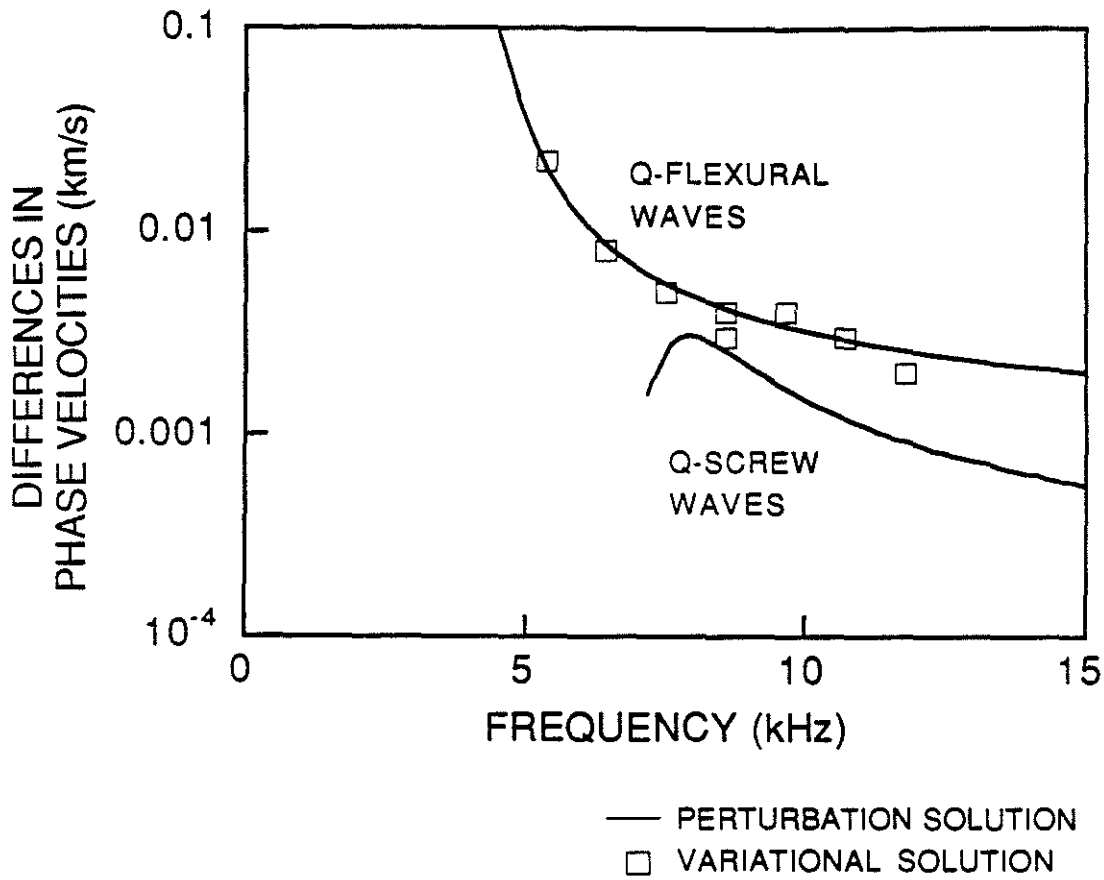

Figure 27: Differences between the phase velocities of the quasi-flexural waves and quasi-screw waves (Figure 21 and 22) in the transversely isotropic model (Table 5) when its symmetry axis is tilted 90° with respect to the borehole. (When differences less than about 0.001 km/s become inaccurate, they are not plotted.)

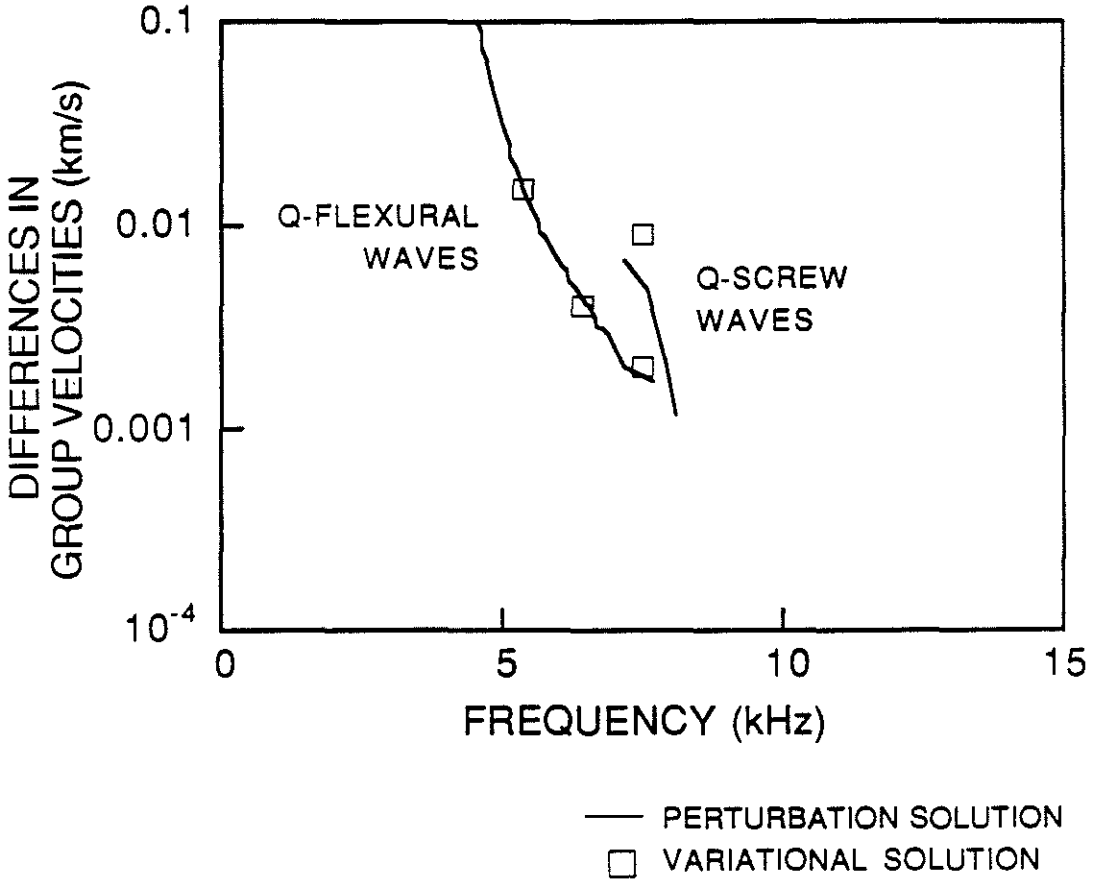

Figure 28: Differences between the group velocities of the quasi-flexural waves and quasi-screw waves (Figure 23 and 24) in the transversely isotropic model (Table 5) when its symmetry axis is tilted 90° with respect to the borehole. (When differences less than about 0.001 km/s become inaccurate, they are not plotted.)

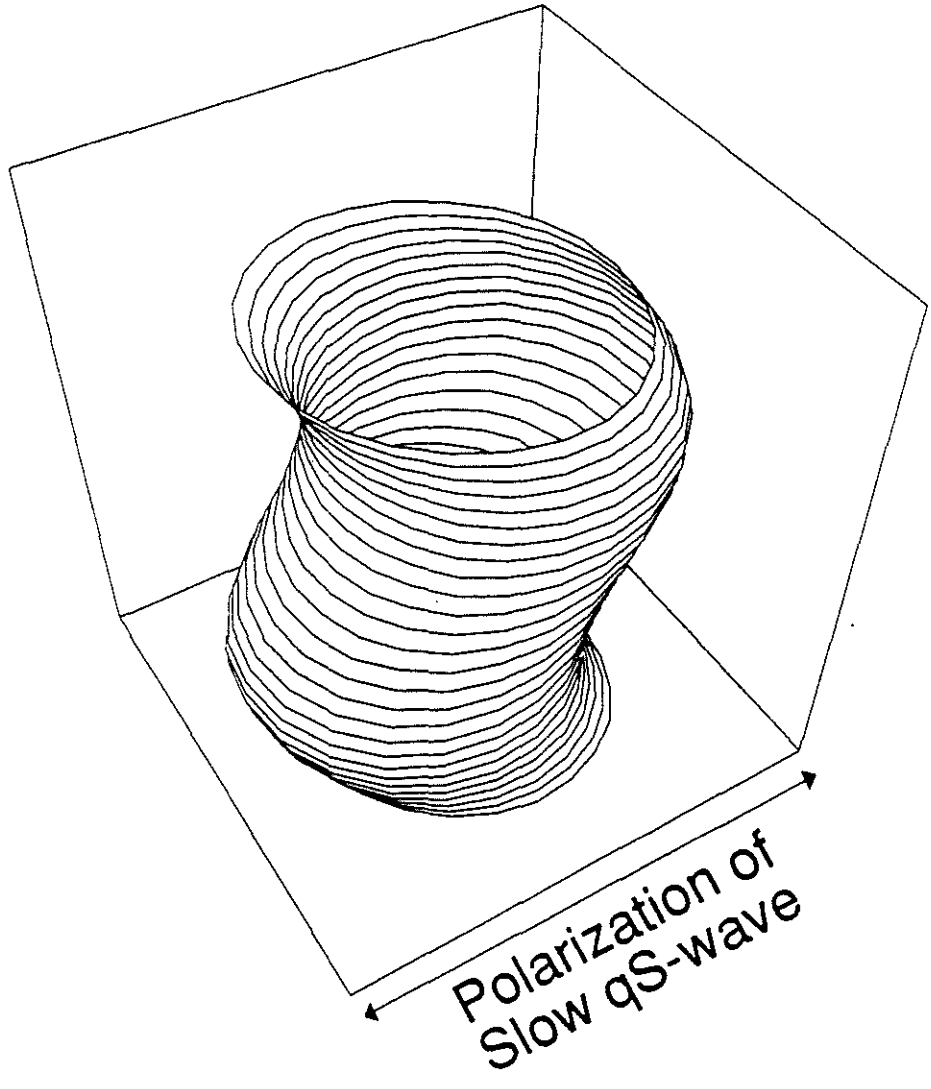

Figure 29: Particle displacements in the r, θ, and z directions for the slow quasi-flexural wave (# 1) at the borehole wall (in the solid and over one wavelength). These displacements were computed for the transversely isotropic model (Table 5) whose symmetry axis is tilted 20°.

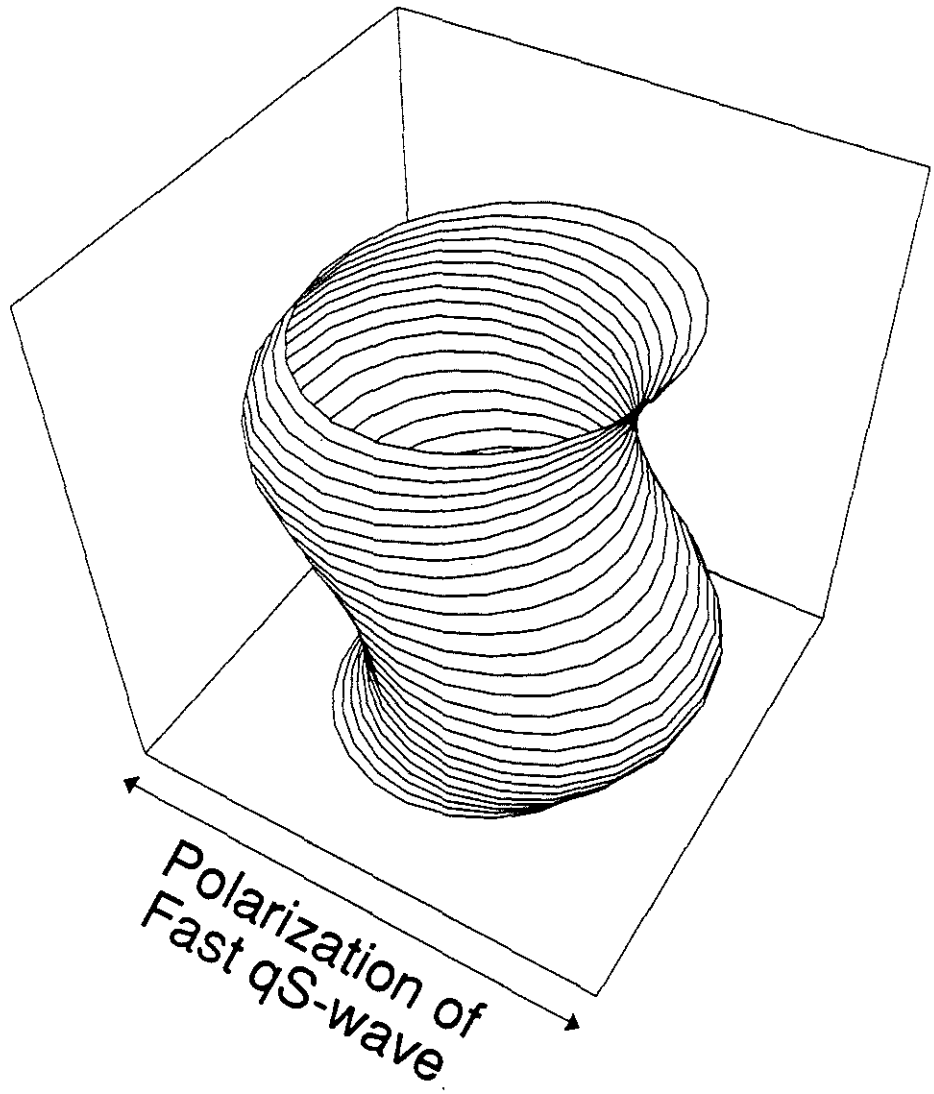

Figure 30: Particle displacements in the r, θ, and z directions for the fast quasi-flexural wave (# 2) at the borehole wall (in the solid and over one wavelength). These displacements were computed for the transversely isotropic model (Table 5) whose symmetry axis is tilted 20°.

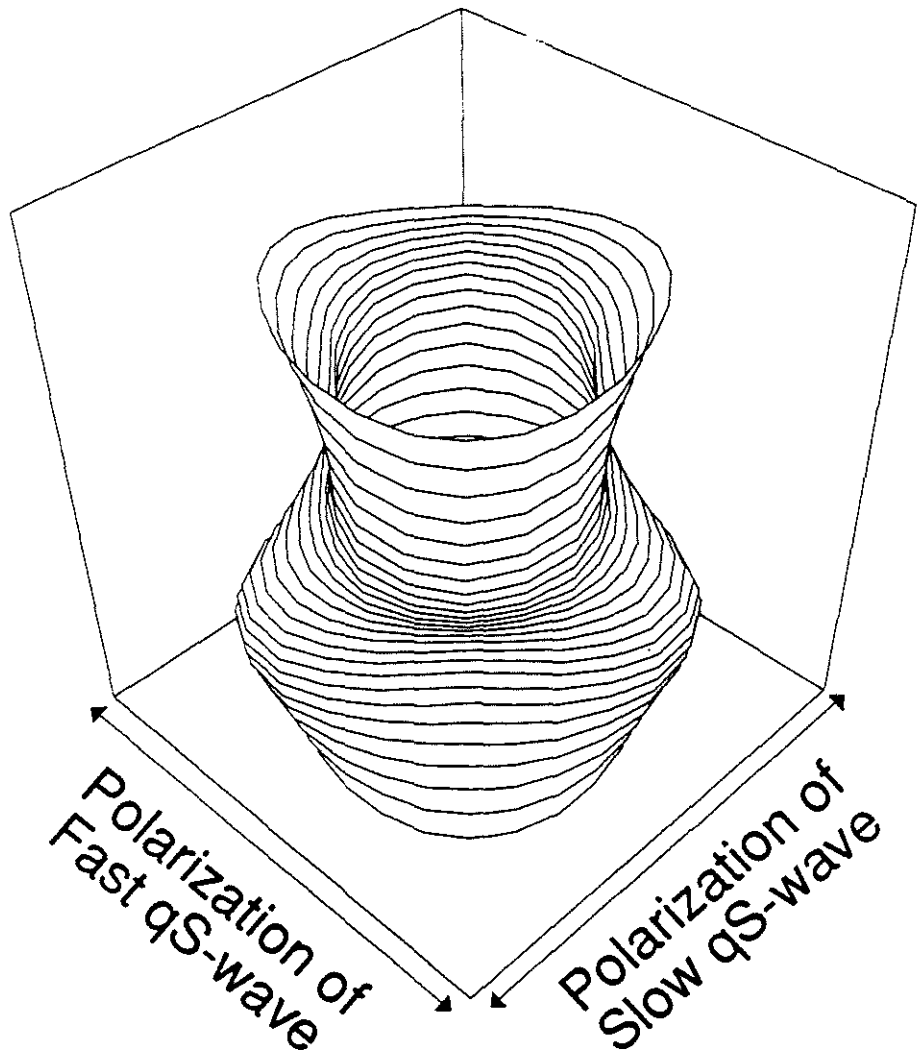

Figure 31: Particle displacements in the r, θ, and z directions for the slow quasi-screw wave (# 1) at the borehole wall (in the solid and over one wavelength). These displacements were computed for the transversely isotropic model (Table 5) whose symmetry axis is tilted 20°.

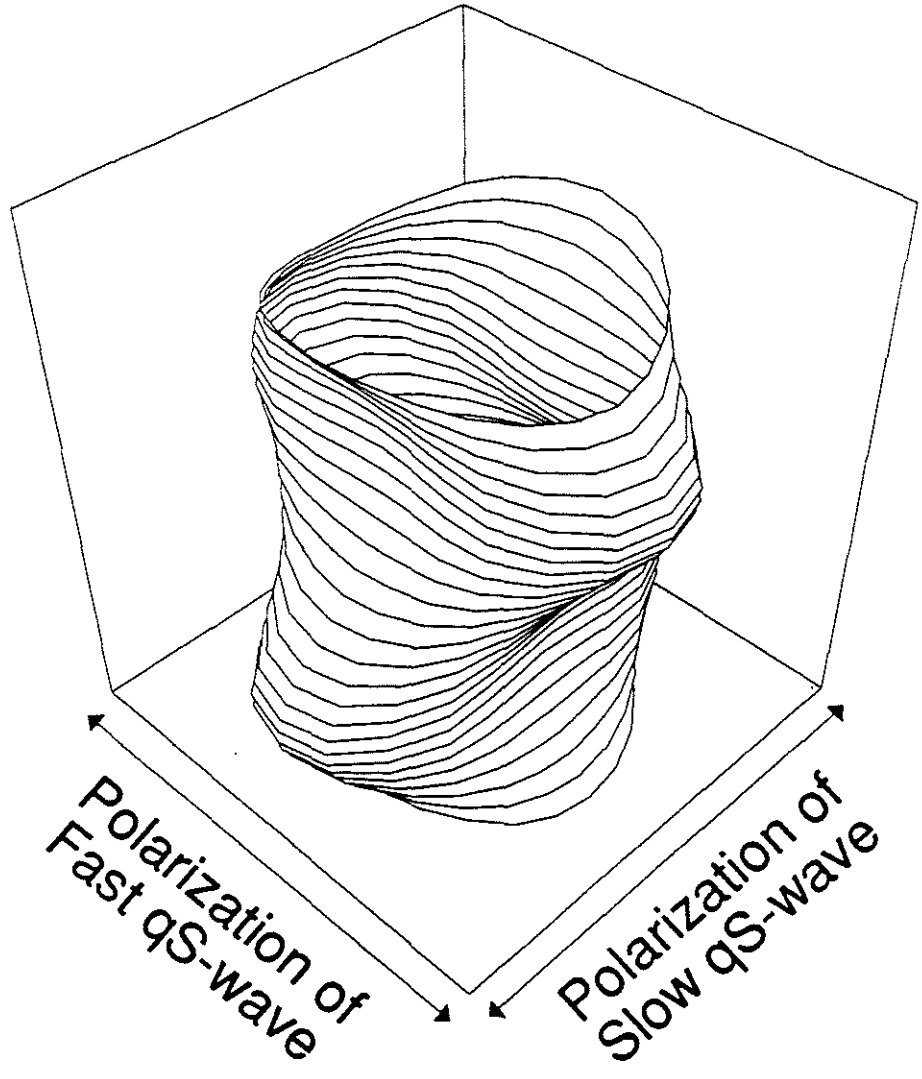

Figure 32: Particle displacements in the r, θ, and z directions for the fast quasi-screw wave (# 2) at the borehole wall (in the solid and over one wavelength). These displacements were computed for the transversely isotropic model (Table 5) whose symmetry axis is tilted 20°.

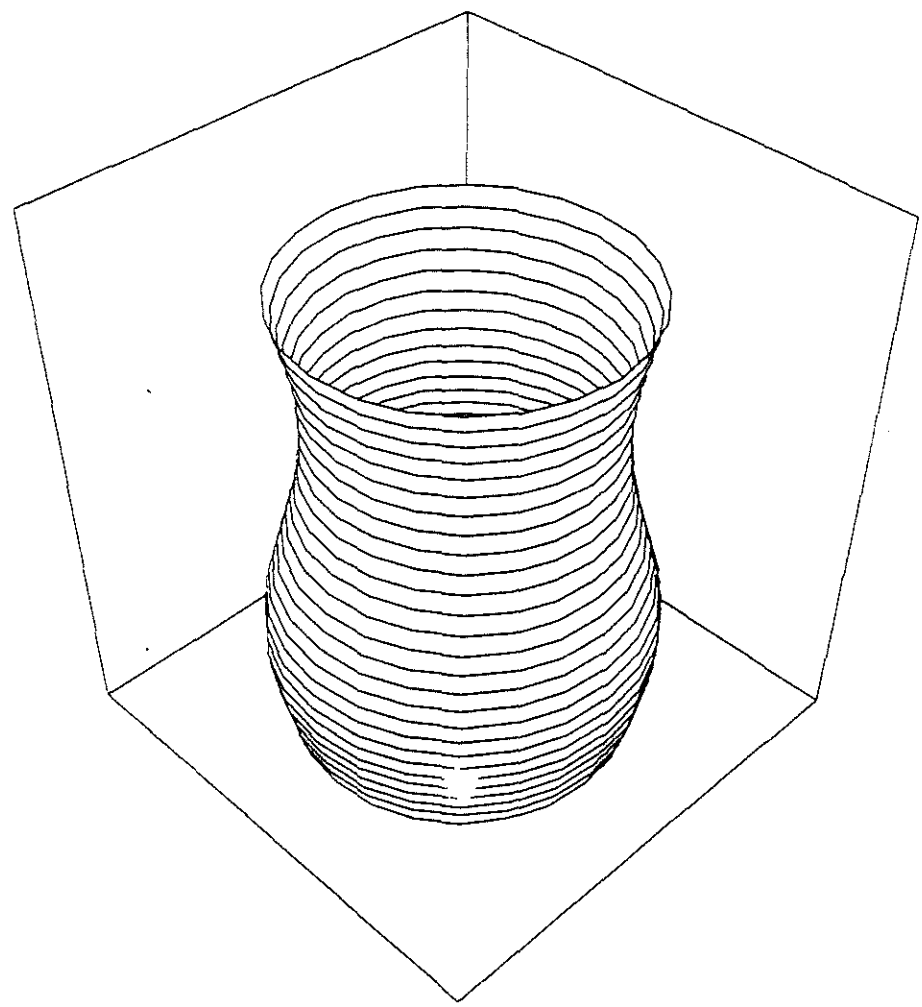

Figure 33: Particle displacements in the r, θ, and z directions for the quasi-tube wave at the borehole wall (in the solid and over one wavelength). These displacements were computed for the transversely isotropic model (Table 5) whose symmetry axis is tilted 20°.

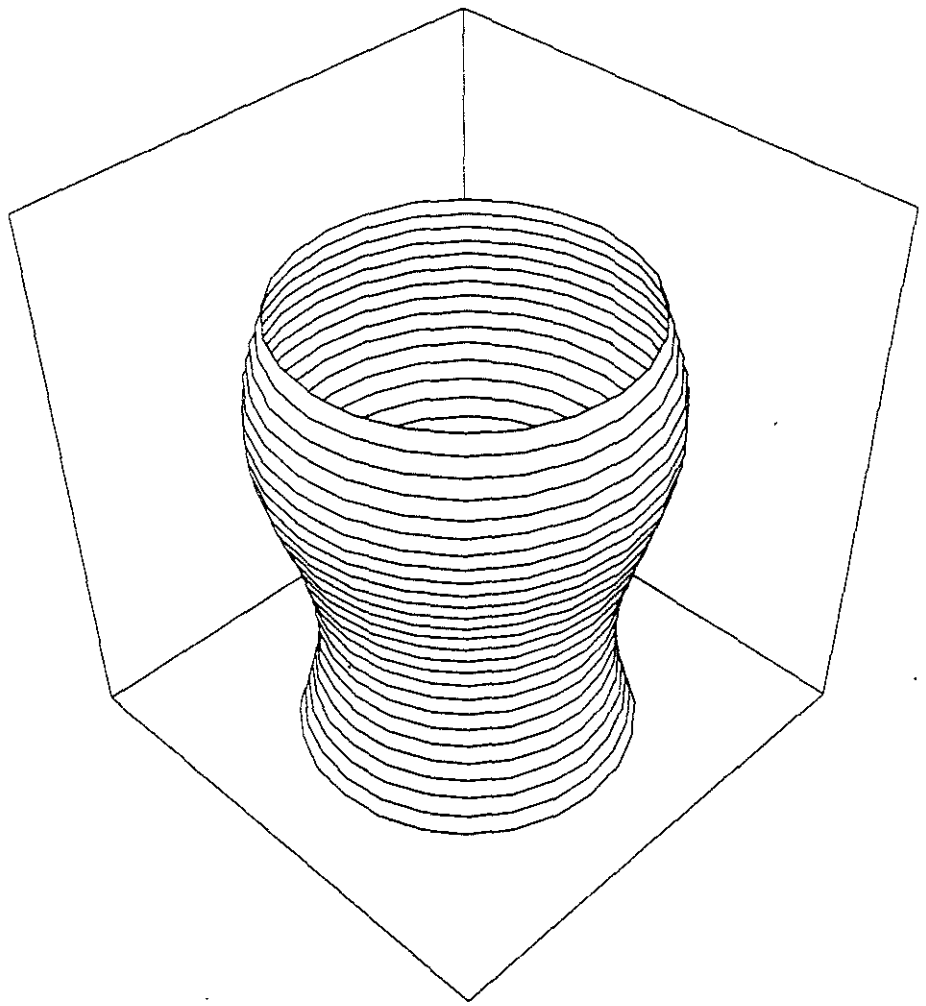

Figure 34: Particle displacements in the r, θ, and z directions for the quasi-pseudo-Rayleigh wave at the borehole wall (in the solid and over one wavelength). These displacements were computed for the transversely isotropic model (Table 5) whose symmetry axis is tilted 20°.

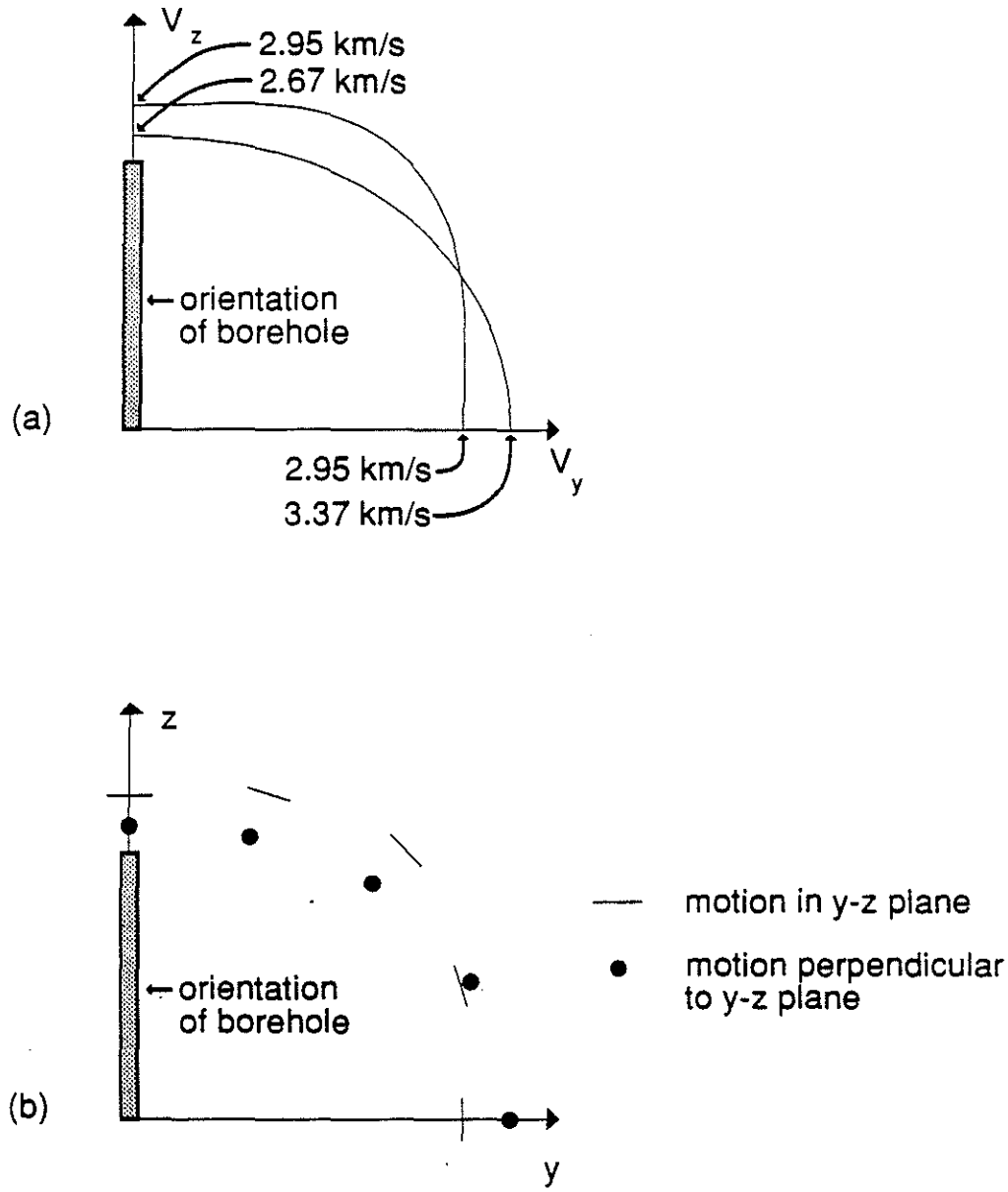

Figure 35: (a) Phase velocity surfaces and (b) polarizations for the qS-waves in the y-z symmetry plane of the orthorhombic model (Table 6).

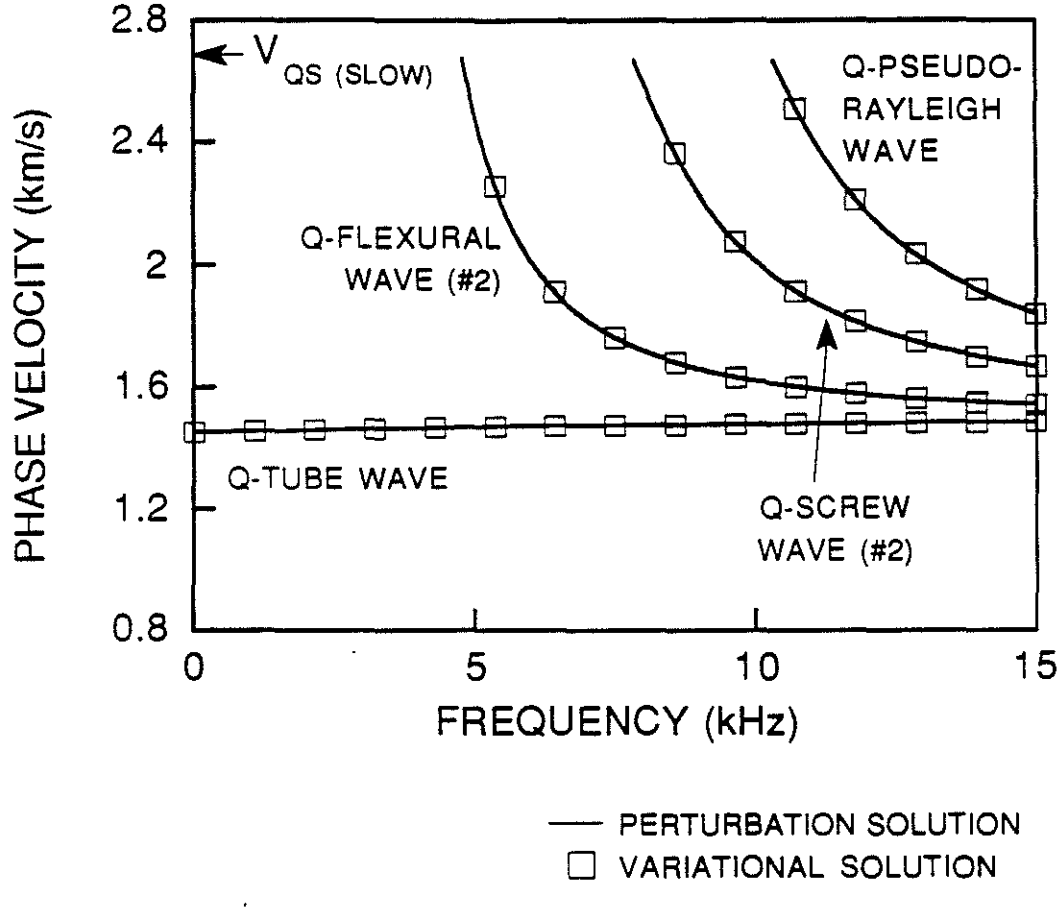

Figure 36: Phase velocities of the normal modes in the orthorhombic model (Table 6). See also Figure 37.

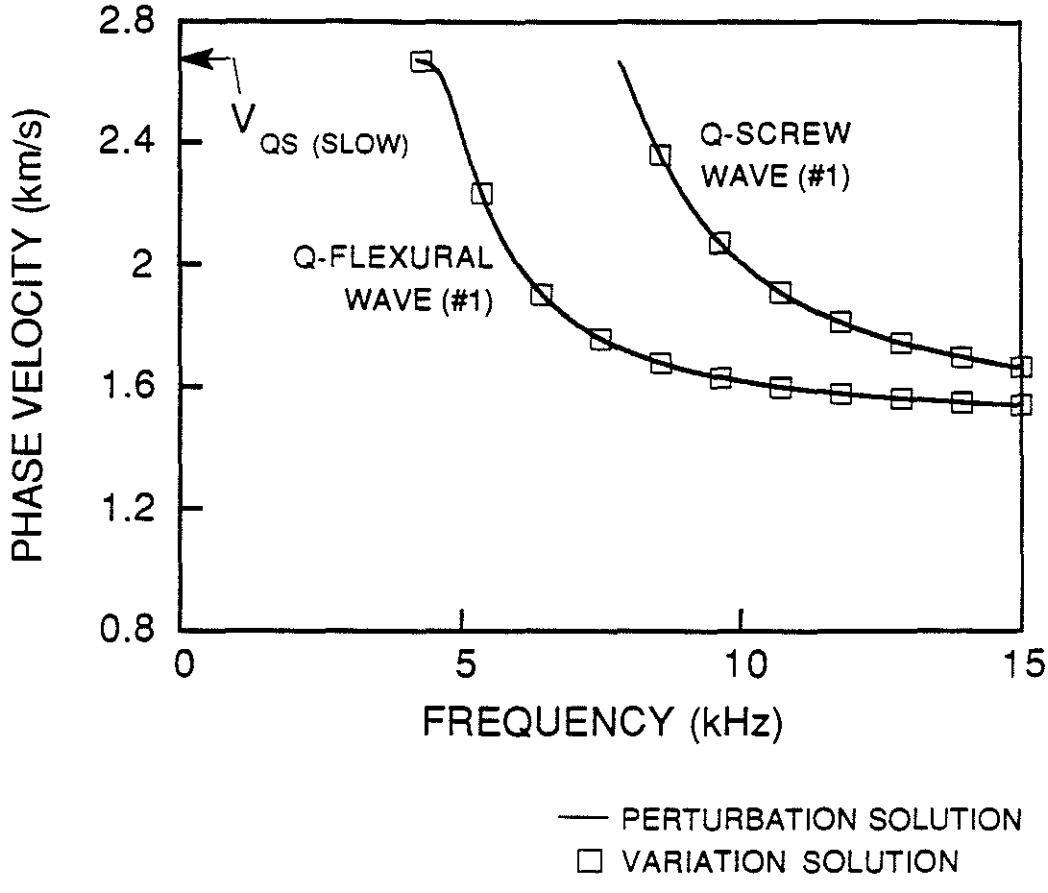

Figure 37: Phase velocities of the normal modes in the orthorhombic model (Table 6). See also Figure 36.

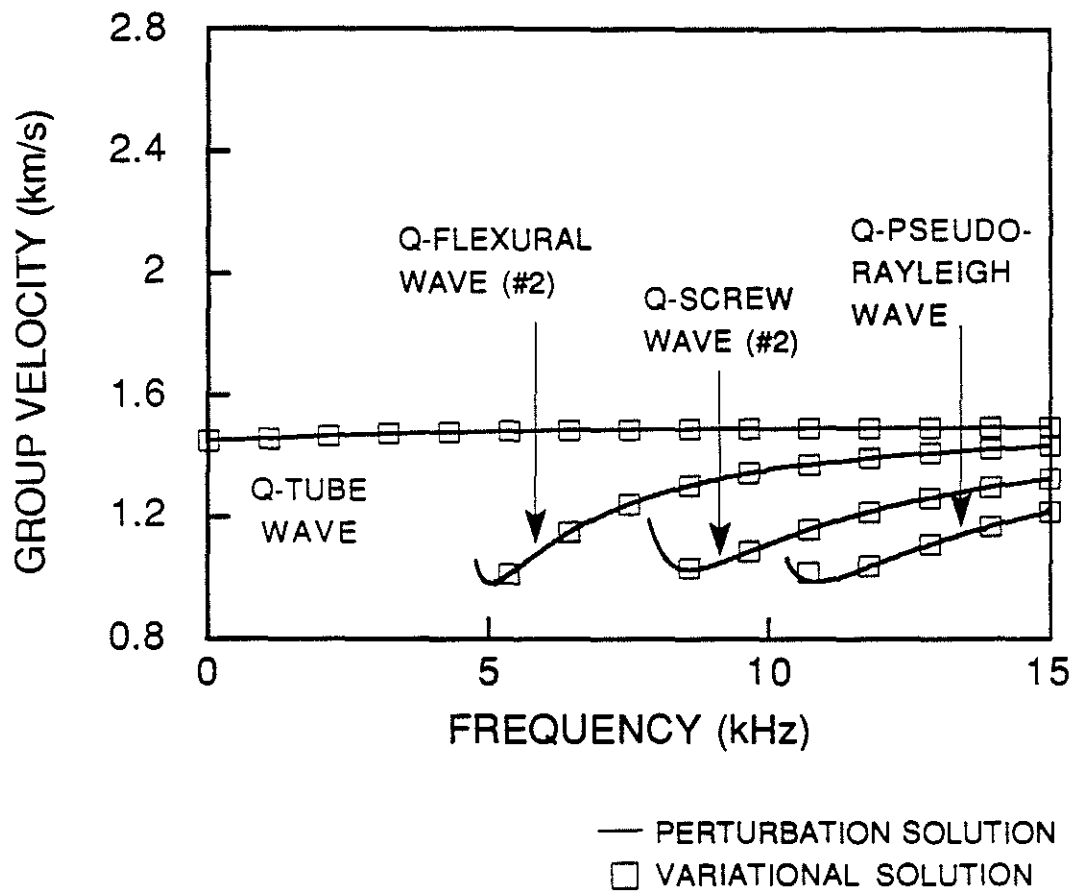

Figure 38: Group velocities of the normal modes in the orthorhombic model (Table 6). See also Figure 39.

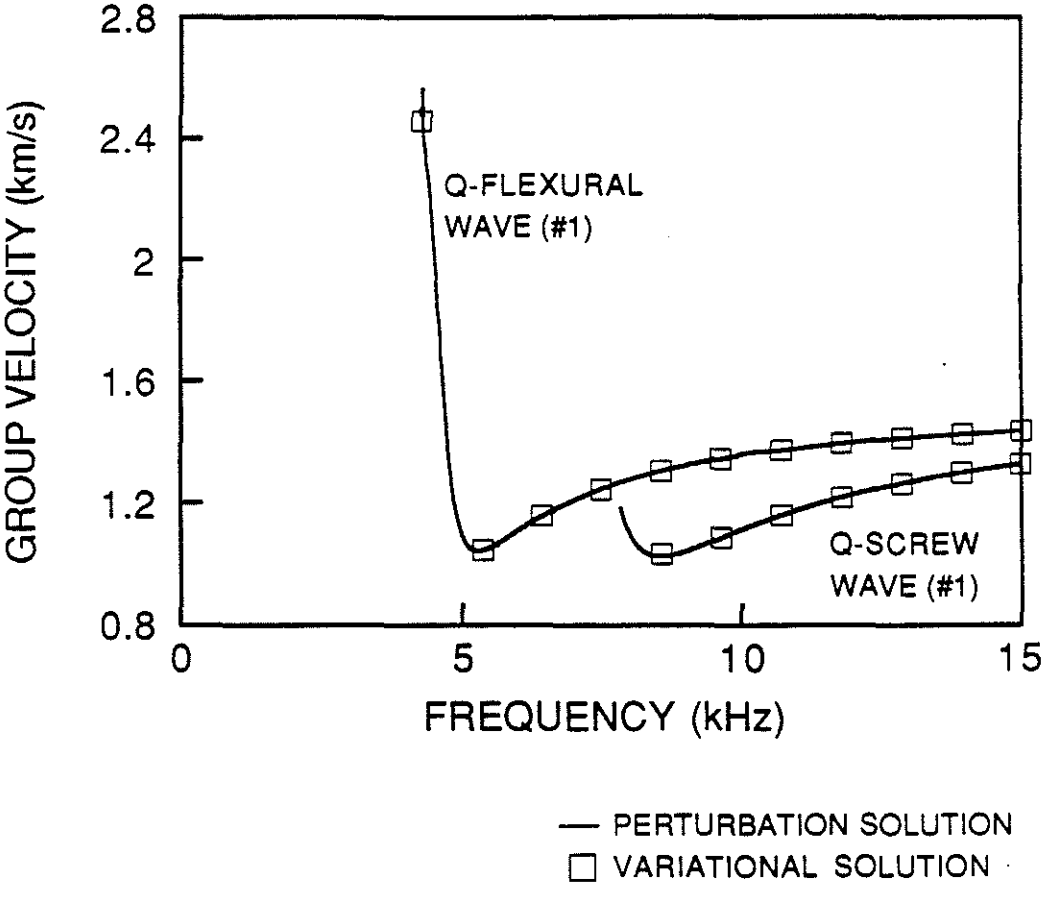

Figure 39: Group velocities of the normal modes in the orthorhombic model (Table 6). See also Figure 38.

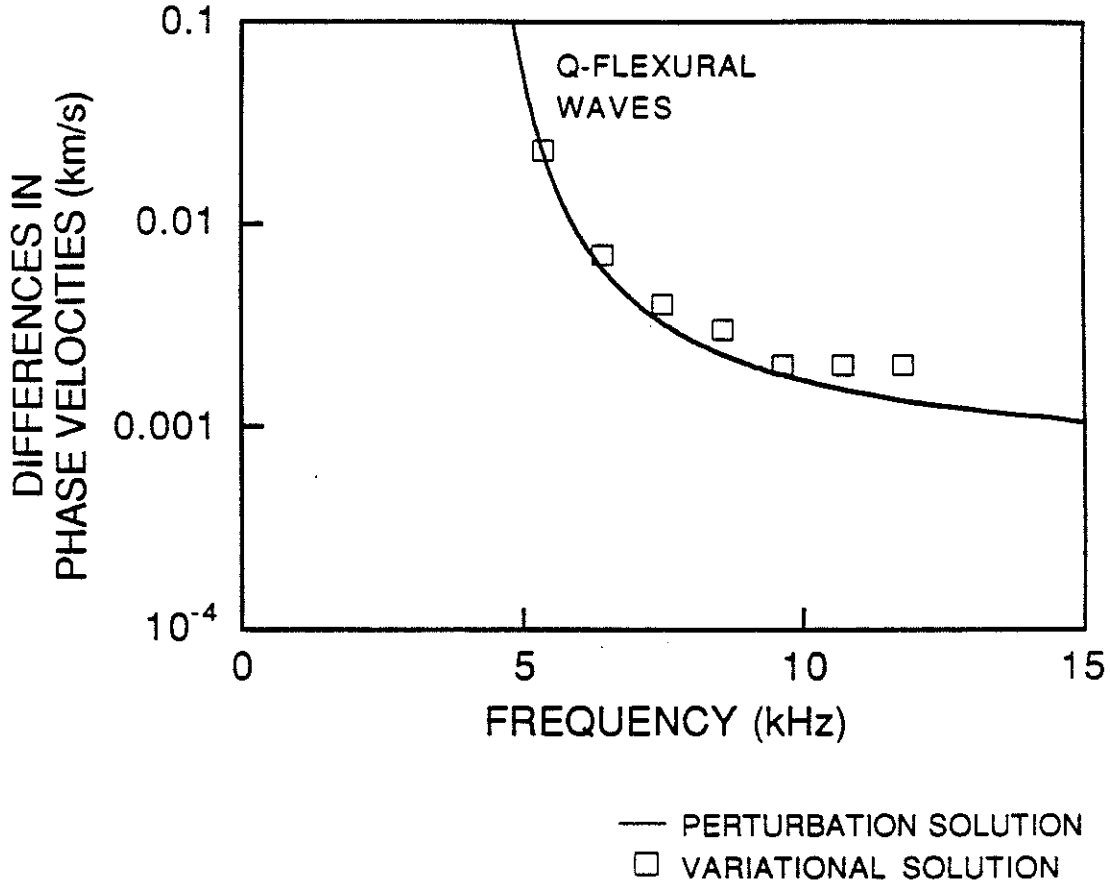

Figure 40: Differences between the phase velocities of the quasi-flexural waves (Figure 36 and 37) in the orthorhombic model (Table 6). (When differences less than about 0.001 km/s become inaccurate, they are not plotted.)

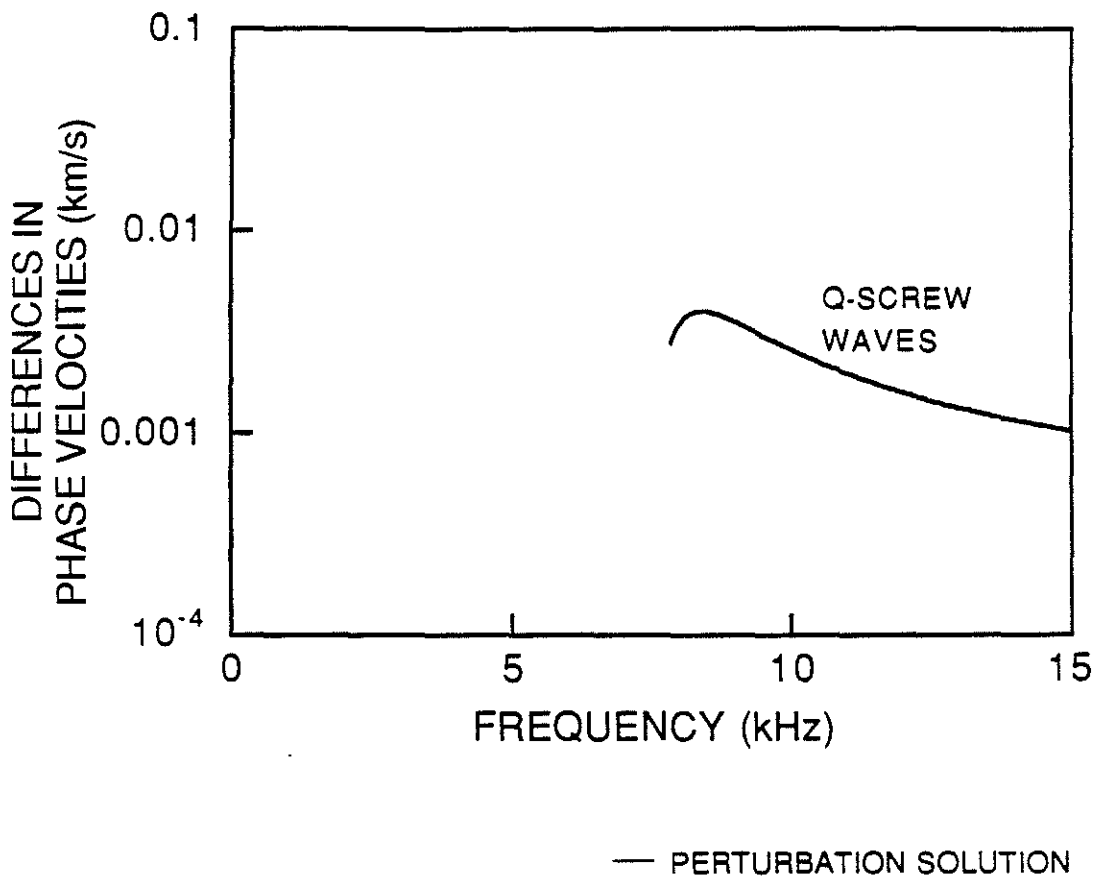

Figure 41: Differences between the phase velocities of the quasi-screw waves (Figure 36 and 37) in the orthorhombic model (Table 6). (When differences less than about 0.001 km/s become inaccurate, they are not plotted.)

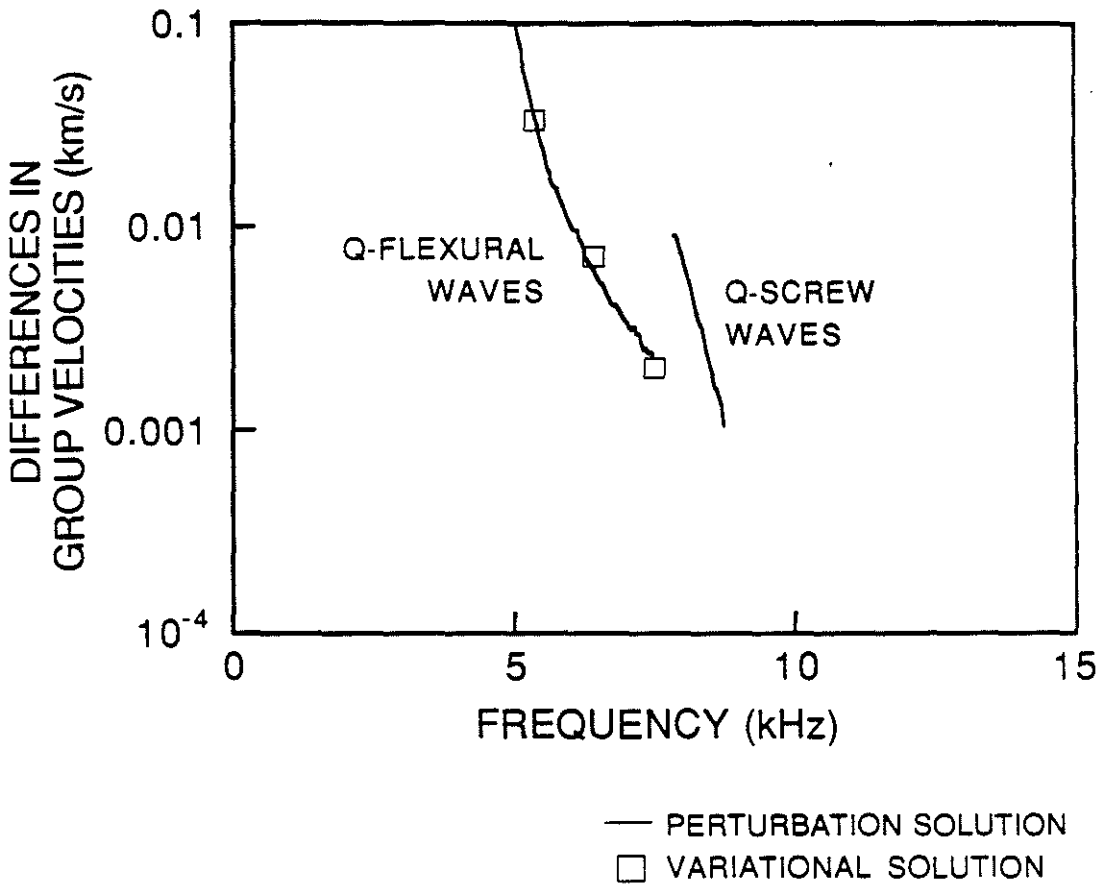

Figure 42: Differences between the group velocities of the quasi-flexural waves and quasi-screw waves (Figure 38 and 39) in the orthorhombic model (Table 6). (When differences less than about 0.001 km/s become inaccurate, they are not plotted.)